



Acker, A. et al. (2020) The CLAS12 Forward Tagger. Nuclear Instruments and Methods in Physics Research. Section A: Accelerators, Spectrometers, Detectors, and Associated Equipment, 959, 163475.

There may be differences between this version and the published version. You are advised to consult the publisher's version if you wish to cite from it.

<http://eprints.gla.ac.uk/208496/>

Deposited on: 16 August 2021

Enlighten – Research publications by members of the University of Glasgow
<http://eprints.gla.ac.uk>

The CLAS12 Forward Tagger

A. Acker^a, D. Attié^a, S. Aune^a, J. Ball^a, P. Baron^a, M. Bashkanov^b, M. Battaglieri^{c,1,*}, R. Behary^d, F. Benmokhtar^d, A. Bersani^c, Q. Bertrand^a, D. Besin^a, T. Bey^a, P. Black^h, P. Bonneau^o, R. Boudouin^a, M. Boyer^a, P. Campero Rojas^o, A. Casale^c, A. Celentano^c, R. Cereseto^c, A. Ciarma^{e,f}, F. Cipro^c, G. Charles^a, G. Christiaens^a, P. Contrepois^a, M. Cook^o, A. D'Angelo^{e,f}, R. De Vita^c, M. Defurne^a, E. Delagnes^a, E. Fanchini^c, S. Fegan^b, J. Fleming^h, A. Filippiⁱ, M. Garçon^a, F. Georges^a, K.L. Giovanetti^j, D.I. Glazier^k, R. Granelli^a, N. Grouas^a, K. Hicks^l, A. Hoebel^o, S.M. Hughes^h, C. Lahonde^a, L. Lanza^{e,f}, M. Leffel^o, T. Lerch^a, T. Lemon^o, K. Livingston^k, A. Manco^c, I. Mandjavidze^a, H. S. Mann^j, B. McKinnon^k, O. Meunier^a, R. Miller^o, G. Mini^c, Y. Mouden^a, P. Musico^c, M. Osipenko^c, G. Ottonello^c, F. Parodi^c, E. Pasyuk^o, P. Pollovio^c, F. Pratolongo^c, S. Procureur^a, R. Puppo^c, C. Rossi^c, M. Riallot^a, M. Ripani^c, A. Rizzo^{e,f}, F. Sabatié^a, C. Salgado^m, G.D. Smith^h, D. Sokhan^k, I. Stankovic^h, M. Taiuti^{c,n}, A. Trovato^c, M. Vandenbroucke^a, E. Virique^a, D. Watts^b, C. Wiggins^o, N. Zachariou^b, L. Zana^o

^aIRFU, CEA, Université Paris-Saclay, F-91191 Gif-sur-Yvette, France

^bUniversity of York, York YO10 5DD, United Kingdom

^cINFN - Sezione di Genova, Via Dodecaneso 33, I-16146 Genova, Italy

^dDuquesne University, Pittsburgh, PA 15282, USA

^eINFN, Sezione di Roma Tor Vergata, 00133 Rome, Italy

^fUniversità di Roma Tor Vergata, 00133 Rome, Italy

^gThe George Washington University, Washington, DC 20052, USA

^hUniversity of Edinburgh, Edinburgh EH9 3FD, United Kingdom

ⁱINFN, Sezione di Torino, 10125 Torino, Italy

^jJames Madison University, Harrisonburg, VA 22807, USA

^kUniversity of Glasgow, Glasgow G12 8QQ, United Kingdom

^lOhio University, Athens, OH 45701, USA

^mNorfolk State University, Norfolk, VA 23504, USA

ⁿUniversità degli Studi di Genova, Via Dodecaneso 33, I-16146 Genova, Italy

^oThomas Jefferson National Accelerator Facility, Newport News, VA 23606, USA

Abstract

This document presents the technical layout and the performance of the CLAS12 Forward Tagger (FT). The FT, composed of an electromagnetic calorimeter based on PbWO₄ crystals (FT-Cal), a scintillation hodoscope (FT-Hodo), and several layers of Micromegas trackers (FT-Trk), has been designed to detect electrons and photons scattered at polar angles from 2° to 5° and to meet the physics goals of the hadron spectroscopy program and other experiments running with the CLAS12 spectrometer in Hall B.

Keywords: Hadron spectroscopy, Low-Q² electron scattering, Electromagnetic calorimeter, PbWO₄, APD, hodoscope, plastic scintillator, WLS fibers, SiPM, gas tracking detector, MicroMegas

1. Introduction

1 An experimental program focused on the search for
2 exotics and the study of rare mesons requires measure-
3 ments of a broad range of final states in order to con-
4 solidate the possible evidence for their production by
5 looking at different decay modes and exploring poorly

7 studied reaction channels [1]. The characteristics of the
8 detector and the trigger conditions foreseen for the ex-
9 periment - 11 GeV electron beam scattering on a 5-cm-
10 long LH₂ target with multiple particles in the final state
11 - will allow measurements of many final states simul-
12 taneously. While the hadrons will be detected in the
13 CLAS12 spectrometer [2], the electron scattered at very
14 small angles (2.5° to 4.5° in polar angle) and low four-
15 momentum transfer, Q², will be detected in the Forward
16 Tagger (FT), i.e. in the kinematics of quasi-real pho-
17 toproduction. The FT specifications were thus defined

*Corresponding author

Email address: marco.battaglieri@ge.infn.it
(M.Battaglieri)

to have optimal electron detection in this angular range, compatible with the high rate of electromagnetic background. To reconstruct the quasi-real photon variables, it is necessary to measure the scattered electron three momentum. The relevant quantities are:

- the energy $E_{e'}$: since the photon energy is given by $E_\gamma = \nu = E_{beam} - E_{e'}$ and its linear polarization by $P_\gamma = \epsilon \sim \left(1 + \frac{\nu^2}{2E_{beam}E_{e'}}\right)^{-1}$,
- the azimuthal angle $\phi_{e'}$ to determine the polarization plane,
- the polar angle $\theta_{e'}$: since $Q^2 = 4E_{beam}E_{e'} \sin^2 \theta_{e'}/2$.

The FT is composed of an electromagnetic calorimeter (FT-Cal) to identify the electron in the energy range 0.5-4.5 GeV by measuring its electromagnetic shower energy and to provide a fast trigger signal, a Micromegas tracker (FT-Trk) to measure the scattering angles ($\theta_{e'}$ and $\phi_{e'}$), and a scintillation counter (FT-Hodo) to provide e/γ separation. The FT-Cal and FT-Hodo also provide fast signals to trigger the data acquisition [3] in coincidence with signals from CLAS12. Figure 1 shows a CAD rendering of the FT.

The calorimeter, the hodoscope, and the tracker are placed between the High Threshold Cherenkov Counter (HTCC) [4] and the torus magnet support [5], at about 185 cm downstream of the nominal target position. The close proximity to the beamline (2.5° corresponds to ~ 8 cm radial distance from the beamline) and the limited space available (at most ~ 40 cm along the beam axis), requires a compact calorimeter of small radiation length and with very good radiation hardness. Figure 2 shows a CAD drawing of the FT integrated in CLAS12. The FT-Hodo, placed in front of the calorimeter, is made of plastic scintillator tiles read-out by silicon photomultipliers via wavelength shifting fibers. The FT-Trk detector is located in front of the FT-Hodo to extend the acceptance of the FT down to 2.5° . All of these components were designed to fit within a 5.5° cone around the beam axis to have minimal impact on the operation and acceptance of the CLAS12 equipment in the forward direction.

2. Detector Layout

2.1. The Calorimeter (FT-Cal)

The FT-Cal has to fulfill demanding requirements in terms of: radiation hardness, light yield, shower containment (small radiation length and Moliere radius),

scintillation decay time, and good energy and time resolution.

The electron energy resolution is a crucial factor to determine precisely the photon energy and to ensure the exclusivity of the measured reaction via the missing mass technique. However, since we are interested in low-energy electrons and high-energy photons, the energy resolution on the latter is significantly better than the resolution of the electron¹. The FT-Cal should have a fast scintillation decay time ($\tau \sim 10$ ns) to sustain high rates with small pile-up effects and to provide the scattered electron interaction time with good accuracy (< 1 ns) in order to reject background and to identify the relevant signals via coincidence with CLAS12.

Due to the expected high rate from electromagnetic background (~ 120 MHz at the nominal luminosity of 10^{35} cm⁻²s⁻¹), the calorimeter should be highly segmented in the transverse direction. The size of each detection element should be comparable with the characteristic transverse size of the electromagnetic shower (Moliere radius) to contain the shower produced by incident electrons to a few readout cells, thus minimizing rates and pile-up. Finally, the photodetectors for the light read out should work in a sizable magnetic field and fit within the available space. Thus, standard photomultipliers (PMTs) cannot be used, while photodetectors based on semiconductors, e.g. avalanche photodiodes (APDs), have been shown to meet the required criteria.

To match the necessary requirements, lead tungstate (PbWO₄) was chosen as the scintillating material and Large-Area APDs (LAAPDs) as the readout sensors. A similar combination was used in the CMS-ECal [7], CLAS-IC [8], and PANDA-EMC [9] calorimeters. Lead tungstate has a fast scintillation decay time (6.5 ns), a small radiation length (0.9 cm), and small Moliere radius (2.1 cm). The drawback of limited light emission (about 0.3% of NaI(Tl)) has been mitigated by using cooled PbWO₄ Type-II crystals (same as used in the PANDA-EMC with better performance with respect to the PbWO₄ Type I used in the CMS-ECal), matched to large-area photosensors to obtain a factor of four more light per MeV of deposited energy than the original CMS-ECal crystals.

With this design, based on GEANT simulations, an energy resolution on the order of $(2\% / \sqrt{E(\text{GeV})} \oplus 1\%)$ is expected. Other crystals, such as LSO/LYSO or the

¹For example, an electron energy resolution of 2% (at 1 GeV) would result in an energy resolution of $\sim 0.2\%$ for the corresponding 10 GeV photon, allowing the use of the missing mass technique for most of the reactions of interest.

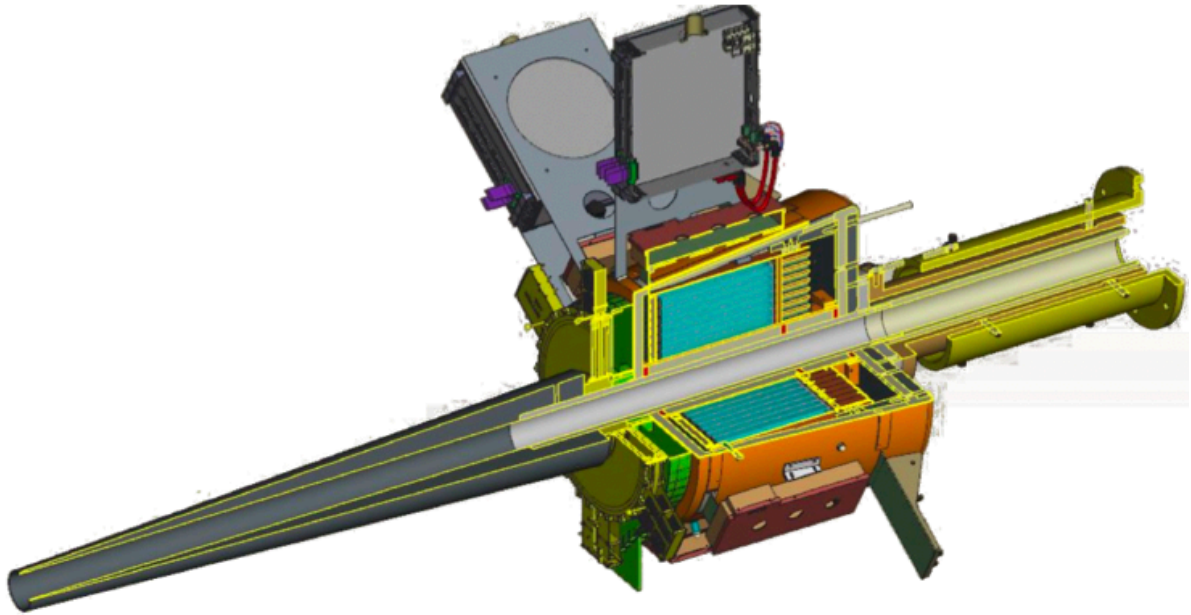


Figure 1: CAD drawing of the Forward Tagger. The FT calorimeter shown in cyan is located at about 185 cm from the beam-target interaction point and is enclosed in a copper and Rohacell case to provide thermal insulation. The scintillation counter (green) and the tracker (yellow) are located in front of the calorimeter. A tungsten cone (gray) shields the FT from Møller electrons and other electromagnetic background (low-energy photons) created by the beam. The left side of this figure represents the upstream end of the detector.

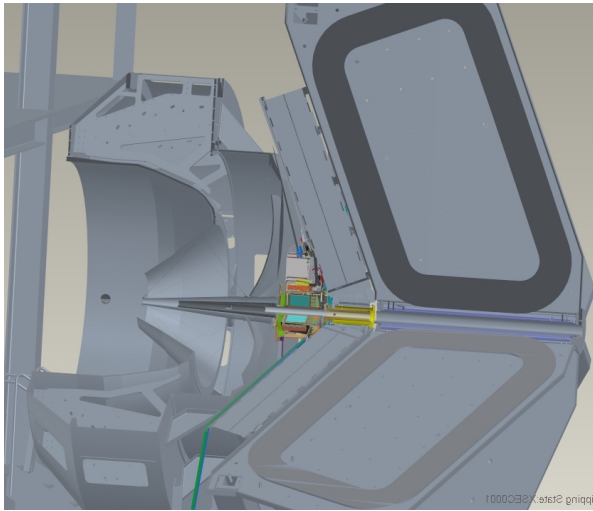


Figure 2: CAD drawing showing the integration of the FT in CLAS12. The FT is located in the free space between the High Threshold Cherenkov Counter (HTCC) [4] and the first Drift Chamber (DC) region [6].

115 from consideration as an alternative.

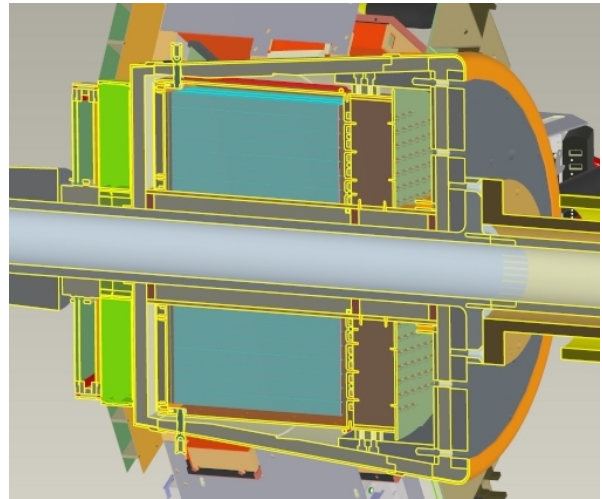


Figure 3: CAD drawing of the FT-Cal showing a cross section of the detector. The crystals, in cyan, are enclosed in the copper thermal shield, in orange, surrounded by insulation, in light gray. On the downstream end of the crystals (right side of the figure), the preamplifiers motherboard is shown in green. The weight of the crystals is supported by the tungsten pipe, in dark gray, which is an integral part of the beamline.

111 very recent LaBr, share almost all of the good specifica-
 112 tions of PbWO_4 with a light yield more than 100 times
 113 larger. However, the higher costs and the limited exper-
 114 ience in the manufacturing procedures excluded them

2.1.1. Geometry and Coverage

The FT-Cal is made from 332 $15 \times 15 \times 200$ mm³ parallelepiped PbWO₄ Type-II crystals arranged around the beamline with full azimuthal angular coverage ($0^\circ < \phi < 360^\circ$) and small forward angle acceptance ($2^\circ < \theta < 5^\circ$). The crystals are placed with their long side parallel to the beamline to form a ring. Figure 3 shows a CAD rendering of the calorimeter.

2.1.2. PbWO₄ Crystals

The FT-Cal PbWO₄ Type-II crystals were produced by the Shanghai Institute of Ceramics, Chinese Academy (SICCAS) [10]. Since the light yield (*LY*) increases when lowering the temperature *T* according to $dLY/dT \sim 3\%/^\circ\text{C}$, the calorimeter is stabilized in temperature and operated at $T \sim 0^\circ\text{C}$ [2]. Lower temperatures were not considered due to significant complications in the mechanical/thermal design, the reduced resistance to radiation, and the decay time degradation of the cooled PbWO₄. The length of the crystals (20 cm - corresponding to ~ 22 radiation lengths) was chosen to minimize the longitudinal loss and to match the available clearance.

The 15 mm \times 15 mm size of the crystal front face provides a pixelization in the transverse plane of the PbWO₄ crystals consistent with the Moliere radius. All crystals were characterized using the ACCOS (Automatic Crystal quality Control System) facility at CERN [11]. The geometrical dimensions, as well as the optical properties such as the longitudinal and transverse transmission and the relative light yield, were determined for each of the crystals. Samples that were outside of the required specifications were rejected and replaced by the manufacturer.

The absolute *LY* (number of detected photoelectrons per MeV deposited) was found to be $N_{pe} = 220 \pm 20$ photoelectrons/MeV at $T = 0^\circ\text{C} \pm 0.5^\circ\text{C}$. For this measurement the crystal was wrapped on 5 of its faces with 3M Vikuiti reflective film and read out by a Hamamatsu S8664-1010 LAAPD operated at a gain $G=150$ connected with optical grease on the exposed face.

The scintillation decay time is also sensitive to the temperature. The time constant was measured using the *Start-Stop* or *Delayed-Coincidence* method at different temperatures. As expected, an increase in the decay constant was observed by decreasing the temperature. At $T = 0^\circ\text{C} \pm 0.5^\circ\text{C}$, we found $\tau = 13.5 \pm 0.6$ ns ($\tau_2 = 11.6 \pm 0.5$ ns and $\tau_1 = 13.0 \pm 0.2$ ns) when a single (double) exponential form was used to fit the data.

²At $T = 0^\circ\text{C}$ the *LY* increases by a factor of two with respect to $T = 25^\circ\text{C}$.

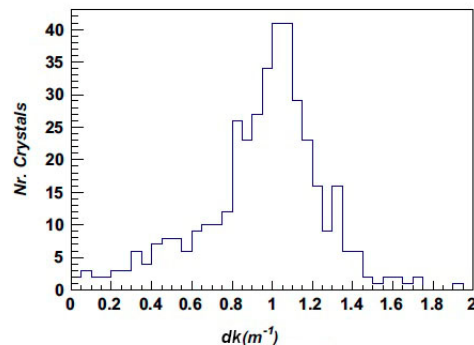


Figure 4: Histogram of the radiation-induced absorption coefficient, dk , for all SICCAS FT-Cal PbWO₄ crystals.

The radiation hardness of the crystals was measured by irradiating them with a dose of 30 Gy of low-energy photons using a ⁶⁰Co source at the Strahlencentrum of Giessen University [12]. The longitudinal transmission was measured before and after the irradiation, calculating the variation as a function of the wavelength. The radiation hardness of the crystals was quantified by the radiation-induced absorption coefficient defined as:

$$dk = \frac{1}{L} \frac{T_{bef}}{T_{irr}}, \quad (1)$$

where T_{bef} is the light transmission at 420 nm, the peak of the PbWO₄ emission spectrum, measured before irradiation, and T_{irr} is the light transmission at the same wavelength after irradiation for crystals of a given length L [3]. Crystals exhibiting greater levels of radiation damage to light transmission have higher values of dk . All 332 crystals assembled in the FT-Cal were individually characterized: on average we found $T_{bef}(420 \text{ nm}) = 61.5 \pm 0.2$ ($\sigma = 3.2$) and $T_{irr}(420 \text{ nm}) = 50.8 \pm 0.5$ ($\sigma = 4.9$). The resulting dk distribution is shown in Fig. 4. These measurements were used to optimize the position of each crystal in the calorimeter, placing the crystals with the highest radiation resistance, and therefore lowest dk , in the areas where the highest radiation dose is expected.

2.1.3. Light Readout and Electronics

The FT-Cal uses 10×10 mm² (model Hamamatsu S8664-1010) LAAPDs to read out the PbWO₄ scintillation light. APDs are only a few mm thick, have a large quantum efficiency at the PbWO₄ light peak emission

³Crystal self-annealing was negligible since the two measurements were performed immediately before and after the short irradiation.

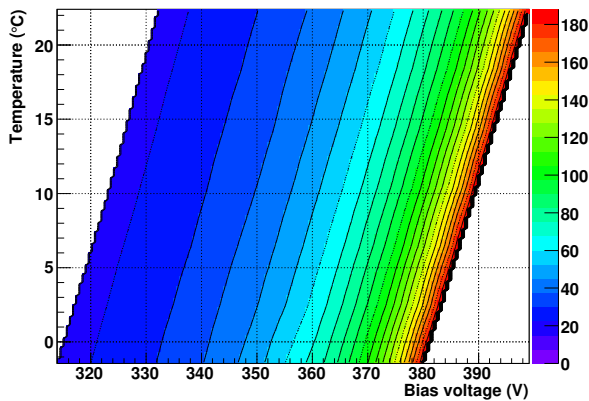


Figure 5: Intrinsic gain of one representative APD as a function of the temperature and bias voltage.

(420 nm), and are insensitive to magnetic fields. The main disadvantage is that, due to their low intrinsic gain (~ 50 -200), the output signal is too small to be directly acquired, and needs to be amplified by a suitable circuit. APDs also need to be operated at a controlled temperature to avoid variations in gain and noise, but this does not represent a major complication since the crystals also are required to be stabilized in temperature. Each sensor used in the FT-Cal has been characterized by measuring its gain as a function of the applied bias voltage at a given temperature using an automated custom facility (see Ref. [13] for more details). The typical gain behavior $G(V_{Bias}, T)$ is shown in Fig. 5. The working point (bias voltage) was chosen in order to have the chosen gain ($G = 150$) in a reasonably stable region for small variations in the biasing. Silicon photomultiplier (SiPM) readout was not considered due to their limited dynamic range, which is not suitable for spectroscopic applications, and the limited experience (in term of reliability, radiation hardness, stability in time, etc.) with their use in large experiments at this time.

The APD current signal is converted to a voltage pulse that is transmitted to the subsequent electronics chain via a transimpedance amplifier (i.e. an amplifier that converts an input current pulse into an output voltage pulse, without performing any time integration). This amplifier has been developed in collaboration with the Service Electronique pour la Physique (SEP) of the Institut de Physique Nucléaire (IPN) in Orsay. The amplifier ENC⁴ was measured at the operating temperature

⁴The ENC, equivalent noise charge, is defined as the charge transported by an input signal giving, at the output of the amplifier, a signal whose amplitude is equal to the RMS of the output noise.

of $T=0^\circ\text{C}$, with $\text{ENC}\sim 10400 e^-$ (RMS) for a nominal gain of $G = 600$. This corresponds to about 3 MeV (RMS) on the measured energy. The amplified signal is read out using the custom JLab flash ADC VME board (a 16-channel, 12-bit, 250-MHz digitizer; referred to as the FADC250). The measurement of the full waveform allows for the derivation of both the charge and time of the hit with the required accuracy.

2.1.4. Light Monitoring System

Lead tungstate scintillating crystals are known as an appropriate material for use in total absorption shower detectors. Unfortunately, although relatively radiation tolerant, their light output is reduced when exposed to electromagnetic radiation and recovers when the radiation source is removed. Further complications arise because at the same irradiation intensity, changes in light output may vary from one crystal to another. In order to maintain the intrinsic energy resolution, the crystals have to be continuously monitored and, if necessary, recalibrated by changing the supply voltage. The monitoring system should be able to test the response over time of the whole chain: crystal, APD, readout electronics. Among the different possible options (radioactive source, laser, and LED) we used an LED-based Light Monitoring System (LMS). In spite of the need for thermal control, LEDs offer the considerable advantage that the matching with crystals is simpler than for lasers, since each crystal can have an LED in front of it and the arrangement of power lines and electrical connections is less critical than for optical fibers. The main disadvantage is related to the complexity of the electronic circuitry. To cover a large light intensity range while maintaining good timing performance, each LED needs a separate driver, which leads for a calorimeter of significant size, to a large number of electronic circuits.

With LEDs it is possible to obtain a shape and a duration of the monitoring-light flash that is similar to the features of the crystal scintillation light. In fact, the emission spectrum of the monitoring light can be chosen to be similar to the radio-luminescence spectrum of PbWO_4 , the effective optical path length for monitoring light in the crystal can be matched to the average path length of the scintillation light produced by an electromagnetic shower, and the pulse length can be tuned to reproduce the PbWO_4 scintillation decay time. We chose a blue light LED with wavelength close to the 430 nm emission peak of the PbWO_4 crystal, where radiation damage may have the maximum effect.

Each crystal is equipped with a separate LED, located on its upstream face, at the opposite end with respect to the light sensors and electronics. The intensity can be

274 varied in the range from 500 to 100,000 photons, pulsed
 275 at a variable rate from 62 Hz to 8 kHz, with a pulse
 276 rise time of ~ 1 ns and a time jitter of less than 200 ps.
 277 The system has been designed to work in the tempera-
 278 ture range from -25°C to $+30^\circ\text{C}$. The LEDs placed in
 279 the closed environment of the crystal are kept at con-
 280 stant temperature with an accuracy of $\Delta T = 0.1^\circ\text{C}$. The
 281 LED monitoring system is split in two boards: one con-
 282 taining the control logic and the LED driver circuits,
 283 and the other, mounted in front of the FT-Cal crystals,
 284 hosting the LEDs. The two boards are connected via a
 285 board-to-board connector that allows the required flex-
 286 ibility to match the FT-Cal geometry and positioning.
 287 The LED drivers are controlled by an on-board PIC32
 288 micro-controller accessible remotely via Ethernet. Each
 289 LED is individually set by a programmable length and
 290 intensity pulse. The system is triggered by an internal
 291 clock or by an external signal. In both cases the trigger
 292 signal is available for a precise time reference.

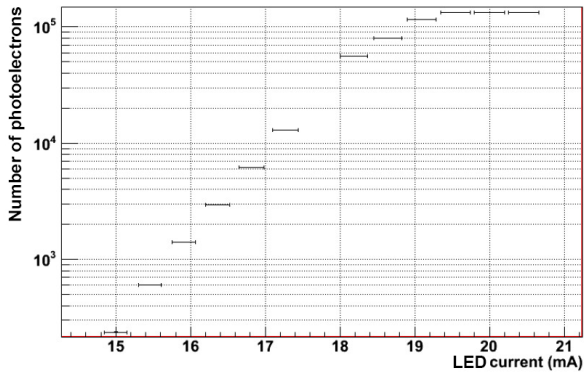


Figure 6: Number of photoelectrons as a function of the LED driver current. The corresponding energy per crystal ranges from 10 MeV to 10 GeV.

293 The performance of the LED driver has been mea-
 294 sured by coupling a single monitoring channel to a
 295 PMT. The performance of the system is reported in
 296 Figs. 6 and 7, where the measured number of photoe-
 297 lectrons as a function of the LED current and the measured
 298 time resolution as a function of the number of photoe-
 299 lectrons are shown⁵. Rescaling the results to take into
 300 account the APD readout and the crystal LY/MeV , the
 301 equivalent energy ranges from 10 MeV (500 photoe-
 302 lectrons - phe) to 10 GeV (500k phe) perfectly match to
 303 the expected energy collected by each crystal. A time
 304 resolution of 100 ps is reached at high light intensity.

⁵The time resolution is defined as the width (σ) of the time differ-
 ence distribution between the trigger signal and the PMT output.

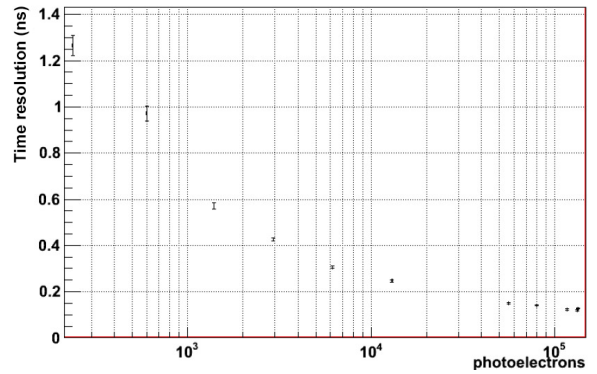


Figure 7: Time resolution (measured as the time difference of the trig-
 ger signal and the PMT pulse) as a function of the LED light intensity.

305 The long-term stability of the system has been measured
 306 over a 100-hr run at $T = +18^\circ\text{C}$. The stability of each
 307 individual channel was found to be in the range of 2%;
 308 when the ratio of any two channels is considered, the
 309 stability is at a level of a few parts per thousand.

2.1.5. Slow Controls and Interlocks

311 The FT-Cal slow controls are part of the CLAS12
 312 EPICS system [3]. The APDs need to be reverse-biased
 313 with a positive high-voltage power source. The APD in-
 314 trinsic gain depends on the bias voltage with $\frac{1}{G} \frac{\Delta G}{\Delta V} \sim 4\%$
 315 and, therefore, the power supply needs to be stable
 316 in time, with low output noise. We chose the CAEN
 317 A1520P board designed for the CMS electromagnetic
 318 calorimeter. The power supply fulfills all of our require-
 319 ments in terms of dynamic range, linearity, and noise.
 320 Each board is equipped with 12 independent channels
 321 that each control a group of 10 APDs with relative gain
 322 variations not greater than 3%.

323 The amplifiers used in the FT-Cal need to be operated
 324 with $+5$ V and -5 V. The power consumption from each
 325 of the two voltage sources is approximately 70 mW, al-
 326 most independent of the event rate, giving a power con-
 327 sumption of ~ 140 mW per board, for a total of 56 W for
 328 a 400-channel calorimeter. The full FT-Cal is powered
 329 by a Wiener MPOD MPV8008L power supply. Sens-
 330 ing feedback is implemented to compensate the voltage
 331 drop across the connecting cables.

332 Temperature regulation is provided by a Lauda
 333 XT150 chiller unit. This is a self-regulating unit and
 334 does not require external feedback, however, the set-
 335 tings and monitored parameters are sent to EPICS for
 336 recording via a *streamDevice* module. The FT-Cal tem-
 337 perature is monitored by a set of PT100 thermoresistors
 338 located at different positions within the crystal assembly

339 and read by a *cRio* module, which is part of the interlock 376
 340 system. The flow of nitrogen gas, which is purged in the 377
 341 preamplifier area to prevent moisture build-up at low 378
 342 temperature, is measured with a flowmeter and moni- 379
 343 tored by the same *cRio* system. The latter is also used to 380
 344 read the output of two humidity sensors located in the 381
 345 preamplifier area. 382

346 The *cRio* system is the main component of the inter- 383
 347 lock system that was designed to provide a fast shut- 384
 348 down mechanism for all critical components in case ab-
 349 normal conditions are detected. The parameters that
 350 are monitored are the FT-Cal temperatures, the nitrogen
 351 flow, and the humidity. If any of the measured values
 352 is found to be outside user-defined ranges, the system
 353 disables the FT-Cal high voltage (HV) and low voltage
 354 (LV) crates and stops the chiller to prevent any damage
 355 to the detector or surrounding elements.

356 2.1.6. Mechanical Design

357 The mechanical design of the calorimeter is driven by
 358 three considerations: minimization of the empty spaces
 359 between the crystals, cooling to 0°C, and optimal cover-
 360 age of the required acceptance without interference with
 361 the rest of CLAS12.



Figure 8: Single crystal assembly: from the left (front) to the right (back), the PEEK support that holds the nose with the LED housing, the crystal wrapped in 3M Vikuiti reflective film, the LAAPD in the PEEK housing, and the preamplifier.

362 The building blocks of the calorimeter are the indi-
 363 vidual lead-tungstate crystals. Each crystal is $15 \times 15 \times$
 364 200 mm^3 , for a weight of 370 g. Each crystal is opti-
 365 cally coupled to an LAAPD on its back face and to an
 366 LMS LED on its front face for calibration. To achieve
 367 the maximum light collection efficiency, the APD covers
 368 almost the entire area of the downstream end of the
 369 crystal, so the LED for monitoring has to be mounted
 370 on the upstream end. This reflects onto the mechan-
 371 ical design of the single-crystal assembly as a mono-
 372 lithic, self-supporting element made of the crystal it- 385
 373 self, the APD, the reflective wrapping, and the crystal 386
 374 support structure. To avoid dead volume in the detec- 387
 375 tor, the mechanical support for each crystal is provided 388

only by the wrapping. We chose 3M Vikuiti reflective
 film. This material is non-conductive, has a reflectiv-
 ity higher than aluminized Mylar and, if properly heat-
 formed, can keep together the different parts of the as-
 sembly. The reflective film is glued on the sides of a
 pair of front/back PEEK custom-machined blocks that
 hold the LAAPD and the LED, respectively. Figure 8
 shows a CAD rendering of the single crystal assembly
 from the front PEEK support to the preamplifier.

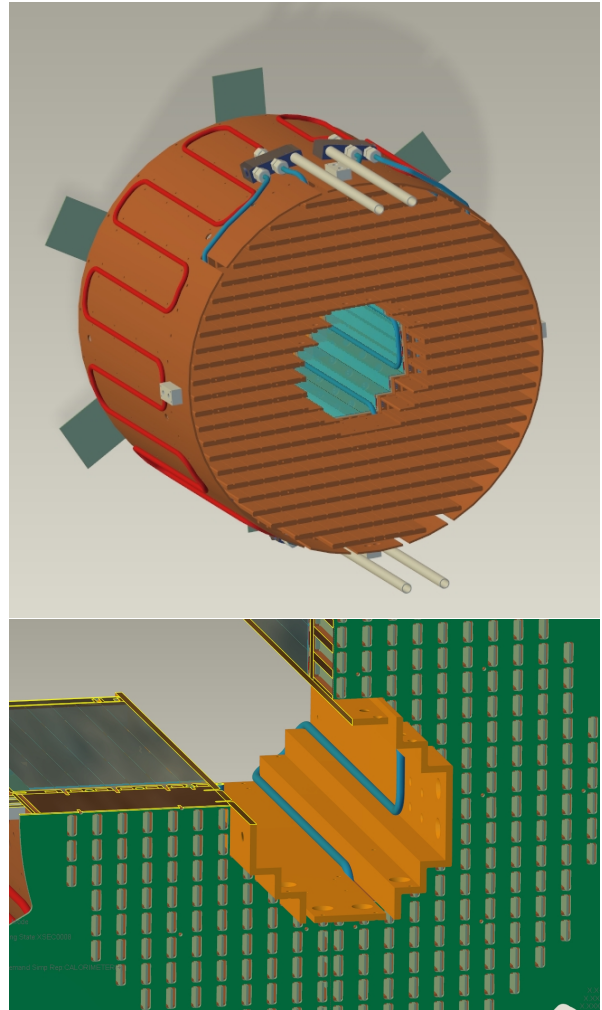


Figure 9: The copper thermal/grounding shield for the FT-Cal. The top figure shows the ensemble of the copper shield with the cooling pipes shown in red and blue. These are located on the back plate, on the outer cylinder, and on the inner shield. The bottom figure shows the cooling pipe circuit inside the inner shield.

The crystal assemblies are installed in a matrix to pro-
 vide complete shower containment for electrons in the
 FT-Cal angular acceptance. Two copper plates, placed
 in front of and on the back of the crystals, define the po-

sitioning for the crystal assemblies. On the APD side, the preamplifiers, one for each crystal, are connected to the readout motherboard, which is designed to provide power distribution and signal collection for each channel. The mechanical structure allows for the replacement of individual preamplifiers if needed. The front and back copper plates are connected by a copper cylinder on the outside and by an inner copper shield to form a closed vessel that surrounds the crystal matrix to provide proper grounding and the required thermal stability and uniformity. Cooling is provided by 5-mm diameter copper pipes installed on the outside of the vessel as shown in Fig. 9.

The FT calorimeter was designed to operate between 0°C and room temperature. The FT-Cal cooling is achieved via circulation of coolant in the circuit attached to the rear copper plate and on the inner and outer copper vessels. The cooling system was designed to compensate the heat load in the region surrounding the FT, taking into account 20 mm of insulating foam (polyisocyanurate thermal conductivity 0.024 W/mK) and from the amplifiers, which dissipate ~50 W. The insulation is less effective between the calorimeter and the inner tungsten pipe that holds the entire FT (see Section 3) because of the limited space for the insulation and the presence of the support structures that bring the overall thermal conductance in that region to 0.056 W/mK.

During the design phase, Finite Element Analysis calculations were performed to optimize the cooling circuit and the insulation parameters in order to reach the design temperature and uniformity. These studies indicated that the coldest part of the external calorimeter enclosure is the tungsten cone, which is expected to stabilize at a temperature just above the dew point. Measurements performed after the calorimeter assembly confirmed these results.

2.2. The Hodoscope (FT-Hodo)

The primary aim of the FT-Hodo is to discriminate between photons and electrons that produce an electromagnetic shower in the calorimeter. Specifically, electrons are identified by hits in the hodoscope array that are correlated in both position and time with a cluster observed in the calorimeter. The FT-Hodo is comprised by an array of 232 plastic scintillator (Eljen-204) tiles segmented in two layers to suppress contributions from the splash-back of the electromagnetic shower created by events depositing energy in the FT-Cal. The scintillators provide fast timing and sufficient resistance to radiation damage for use in the high-rate and high-dose environment of the FT. The geometry and readout of

the hodoscope are constrained by the surrounding apparatus. Specifically, the device is positioned upstream of the FT-Cal, fitting into a circular disk of diameter 330 mm and 42 mm depth. The readout is achieved using 3×3 mm² Hamamatsu S13360-3075PE SiPMs (50% photon detection efficiency for 450 nm photons) coupled to 5-m-long clear optical fibers (Kuraray clear-PSM with attenuation length > 10 m), which are fusion spliced to ~30-cm-long wavelength shifting (WLS) Kuraray Y11 fibers (attenuation length of > 3.5 m), embedded in the scintillator tiles. The splicing induces a photon loss of less than 2%, where the use of optical fibers allows the captured light to be transported with a light loss of less than ~40% over the 5-m path to the SiPM. This readout design of the FT-Hodo addresses the need to minimize material in the detector acceptance, to operate in regions of high magnetic fields produced by the CLAS12 solenoid and torus magnets, and to tolerate the high-background radiation environment.

Each layer of the FT-Hodo is comprised of 44 15 mm×15 mm (P15) and 72 30 mm×30 mm (P30) scintillators arranged as shown in Fig. 10. The upstream and downstream layers utilize 7-mm and 15-mm-thick scintillator tiles, respectively. The upstream (thin) layer is employed to reduce photon conversion in the FT-Hodo, while the thicker layer provides the signal with the most accurate timing information for the event. To increase the number of scintillation photons collected from each tile, four WLS fibers were embedded in the P30 tiles and 2 in the P15 tiles. In addition, the WLS fibers were glued with Epotek 301-2 glue inside diagonal holes to maximize the path length in the scintillator and to allow for the tiles to be arranged without any dead space between the elements.

Each tile was polished and painted with two layers of Bicon BC-620 reflective paint for the sides and 3 layers for the scintillator faces and secured in position on the surface of a 1-mm-thick plastic support board. There is a 9-mm clearance for each layer for routing the optical fibers to the readout electronics through a Δ -shaped sheathing on the bottom end of the FT-Hodo. The front and back faces are covered by light-proof carbon fiber material that is screwed onto supporting structures made out of hexagonal plastic spacers (15-mm wide and 22- or 15-mm tall depending on the layer). This results in a total detector thickness of 42 mm. A 1-mm-thick plastic strip traces the outer contour of the FT-Hodo and is glued onto the spacer supports. Figure 11 shows a CAD drawing of the FT-Hodo highlighting one layer of tiles, the location of the plastic supports for the light-proofing structure, and the plastic strip.

With the typical maximum radiation doses deter-

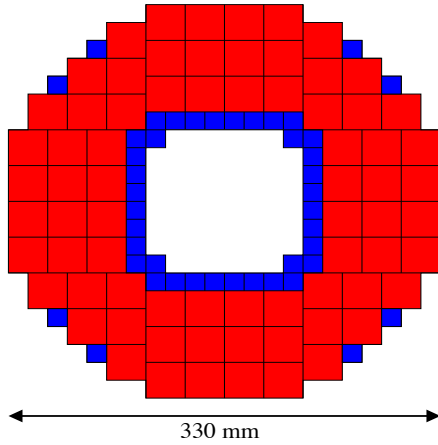


Figure 10: The arrangement of plastic scintillator tiles in the FT-Hodo. The blue (red) squares represent the 15 mm×15 mm (30 mm×30 mm) tiles for each layer.

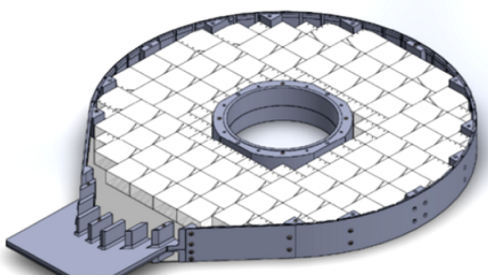


Figure 11: CAD drawing of the FT-Hodo showing one layer of tiles, the locations of the plastic spacers, and the plastic strip that traces the outer contour.

491 mined through Geant4 simulations with realistic beam
 492 and target parameters, and without the shielding effects
 493 of the Møller cone (see Section 3), the FT-Hodo will
 494 experience a light loss of 20% in the WLS fibers after
 495 3.5 years, whereas the plastic scintillators will expe-
 496 rience a light loss of 20% after 300 years [14]. Both
 497 scintillators and fibers also show natural annealing pro-
 498 cesses, which can effectively compensate for the radia-
 499 tion damage [14].

500 The analog signal from the SiPM is fed directly to
 501 a custom-designed preamplifier board designed by the
 502 INFN-Genova Electronics Group. The boards host 8 in-
 503 dependent channels, each coupled to a SiPM and are
 504 mounted in pairs in the slots of a custom crate, me-
 505 chanically compatible with the VME standard. The 16
 506 SiPMs connected to each pair of boards are mounted on
 507 a mezzanine printed circuit board, which distributes the
 508 bias HV to each SiPM and collects their signals for the
 509 amplifier inputs. The schematic of one channel of the

510 SiPM amplifier board, excluding the HV bias network
 511 is shown in Fig. 12. The first stage is based on a bipolar
 512 junction NPN transistor in a common base configura-
 513 tion, while the second is composed of an OPA694 opera-
 514 tional amplifier in a non-inverting configuration. The
 515 two BFR92 transistors have been chosen since they are
 516 low-noise transistors with a high cut-off frequency and
 517 good stability. The two stages are coupled together with
 518 a 100 nF capacitor to remove the DC component of the
 519 signal from the second transistor. The amplifier is cou-
 520 pled to the output connector through a 100 nF capacitor
 521 and a 50 Ω resistor to remove any DC component from
 522 the last stage, and to match the impedance of the output
 523 cable.

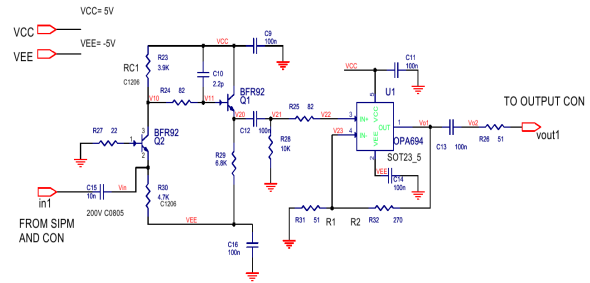


Figure 12: Schematic of a single channel of the amplifier board for the SiPM.

524 The signal from each SiPM after amplification is con-
 525 tinuously digitized by the JLab FADC250 boards and,
 526 if the trigger condition is satisfied, samples are stored
 527 for further analysis. The data acquisition and slow con-
 528 trols system for the FT-Hodo are similar to the FT-Cal
 529 (see Section 2.1.3 for more details). The SiPMs operate
 530 with a bias voltage of 50-55.5 V, which is provided by
 531 three CAEN A1737P HV boards. 30 independent HV
 532 channels are used to operate each SiPM board that host
 533 8 sensors. These groups of 8 SiPMs were selected ac-
 534 cording to their gain. The HV distribution to the groups
 535 of 8 SiPMs is implemented on the mezzanine boards
 536 that also hosts a compensation circuit to allow for the
 537 independent regulation of each SiPM bias voltage up
 538 to a maximum of 0.4 V. The low voltage system used
 539 for the FT-Hodo is the same as the one used for FT-Cal.
 540 Controls of both the HV and LV for the detector are pro-
 541 vided by the CLAS12 EPICS slow controls system [3].
 542 Similarly to the FT-Cal, the status of the critical com-
 543 ponents, in this case the temperature of the preamplifier
 544 crate, is incorporated into the interlock system that is
 545 programmed to disable the HV and LV crates if abnor-
 546 mal conditions are detected.

547 **2.3. The Micromegas Tracker (FT-Trk)**

548 For a precise determination of the scattered elec-
 549 tron angle, a tracker complements the FT-Cal and FT-
 550 Hodo detectors. The FT-Trk uses the same technol-
 551 ogy adopted by the CLAS12 central and forward Mi-
 552 cromegas detectors. We refer to Ref. [15] for a detailed
 553 description of these devices. In this section we describe
 554 the specific design of the FT-Trk.

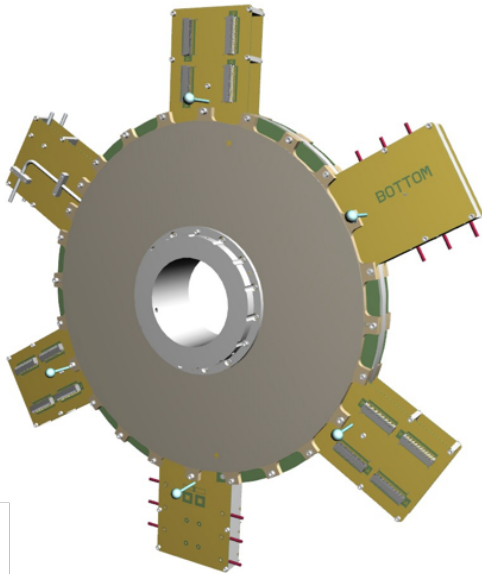


Figure 13: 3D view of the upstream face of the FT-Trk Micromegas tracker equipped with front-end electronics.

555 Two double-layers of Micromegas detectors are lo-
 556 cated in front of the hodoscope, in the space between
 557 the FT and the HTCC [4]. The two detectors are indeed
 558 a good compromise to achieve an efficient background
 559 rejection and track reconstruction with a low material
 560 budget. Each layer is composed of a double-faced Mi-
 561 cromegas disk built on a common printed circuit board
 562 (PCB). Each side of the PCB displays strips, the down-
 563 stream strips being perpendicularly oriented to the up-
 564 stream strips. This particular geometry enables the de-
 565 termination of the (x, y) coordinates (perpendicular to
 566 the beam z -axis) of a track. To limit the number of elec-
 567 tronics channels, the pitch chosen was $500 \mu\text{m}$, which
 568 leads to a resolution better than $500/\sqrt{12} \sim 150 \mu\text{m}$. A
 569 drift space of 5 mm , together with an amplification gap
 570 of $128 \mu\text{m}$, provides good efficiency. The two double-
 571 layers, centered on the beam axis, cover polar angles
 572 from 2.5° to 4.5° with an active area defined between
 573 a 70 mm inner radius and a 143 mm outer radius. The
 574 total number of channels is 3072. Figure [13] shows the

575 CAD implementation of the detector. The FT-Trk read-
 576 out uses the same data acquisition scheme adopted for
 577 the CLAS12 Barrel Micromegas Tracker (BMT) [15],
 578 which consists of a Front-End Unit (FEU) and a Back-
 579 End Unit (BEU).

580 The front-end electronics are responsible for signal
 581 preamplification, shaping, buffering during the trigger
 582 generation process, data digitization, and compression.
 583 Due to the limited space available, the front-end elec-
 584 tronics are designed to be placed off-detector. Micro-
 585 coaxial cable assemblies connect the detectors and the
 586 front-end boards. The non-amplified analog signals
 587 transit via the cable assemblies from the chambers to
 588 the front-end electronics. The 512-channel FEUs are
 589 housed in 4U crates attached to the FT-Cal mechanical
 590 supports, which are located in the geometrical shadow
 591 of the CLAS12 torus coils. The back-end electronics are
 592 responsible for data concentration, providing the inter-
 593 face to the CLAS12 event building system and are the
 594 same units used for the BMT [15].

595 Each Micromegas layer is powered with 450 V for the
 596 micro-mesh and 1000 V for the drift electrode. The FT-
 597 Trk front-end power supply is located 12 m away from
 598 the crates. The 15 W power produced by each crate
 599 is dissipated by compressed air. An interlock system
 600 between the cooling infrastructure and the low voltage
 601 power supply prevents powering the front-end crates
 602 when cooling is off.

603 The gas used is a mixture of argon, isobutane (up to
 604 10%), and CF_4 (up to 5%). The use of CF_4 ensures good
 605 time resolution (around $10\text{-}15 \text{ ns}$). The gas distribution
 606 system is the same one used by the BMT.

607 **3. Integration in CLAS12**

608 The FT mechanical design was driven by the geo-
 609 metrical constraints imposed by the other CLAS12 sub-
 610 detectors, geometrical acceptance optimization, and
 611 performance optimization, taking into account the cool-
 612 ing requirements, material budget, and front-end elec-
 613 tronics location. The FT detects electrons scattered be-
 614 tween 2.5° and 4.5° with respect to the beam axis. To
 615 provide this acceptance, the FT calorimeter must cover
 616 down to 2° and up to 5° with lead tungstate crystals
 617 to have a good containment of electromagnetic showers at
 618 the edges of the polar angular range. Since no massive
 619 materials are allowed at angles larger than 5.5° , the crys-
 620 tals, cooling system, mechanical supports, and tungsten
 621 shielding have been optimized in a very compact design.
 622 Outside of 5.5° the only materials are very low-density
 623 (35 kg/m^3) insulation and routing for cabling and ser-

624 vices in the geometrical shadow of the CLAS12 detector
 625 where the torus magnet coils are located.

626 The FT is built from several components that can be
 627 grouped as follows:

- 628 • the inner tungsten pipe,
- 629 • the tungsten cone acting as a Møller electron
630 shield,
- 631 • the FT-Trk tracker,
- 632 • the FT-Hodo hodoscope,
- 633 • the FT-Cal calorimeter,
- 634 • the front-end electronics,
- 635 • cabling and services.

636 From the mechanical point of view, the most chal-
 637 lenging aspect is the integration of the calorimeter, due
 638 to the weight and fragility of the crystals, and the rela-
 639 tive positioning and alignment of the FT components.

640 3.1. Constraints from Other Sub-detectors

641 The FT must be centered on the beamline between
 642 the HTCC and the first set of the DCs [6]. The HTCC
 643 can be retracted in the upstream direction to give access
 644 to the FT. In its operating position, the HTCC extends to
 645 1730 mm downstream with respect to the nominal tar-
 646 get center. This forms a plane that defines the upstream
 647 edge of the space allowed for the FT. The first set of
 648 DCs is installed in front of the coils of the torus magnet,
 649 with an inclination of 65° with respect to the beam axis.
 650 The front-end electronics boards of the DCs define the
 651 downstream border of the space allowance for the FT.
 652 The minimum distance of the DC boards from the beam
 653 axis is ~ 140 mm at 2280 mm downstream with respect
 654 to the nominal center of the target. Taking into account
 655 the outside radius of the FT, including its insulation and
 656 the inclination angle of the DCs, the downstream face
 657 of the FT cannot exceed ~ 2150 mm with respect to the
 658 nominal center of the target.

659 The FT needs cabling and service routing for the gas
 660 and cooling lines. These services must be connected
 661 to the outside of CLAS12. All services are installed in
 662 the shadow area of the torus magnet coils, i.e. in the
 663 six azimuthal slots extending radially from the beamline
 664 to the periphery. Each coil is ~ 100 -mm thick, which
 665 allows space to host some front-end electronics for the
 666 FT, which must be close to the detectors.

667 The whole FT is attached to the torus magnet cryostat
 668 by a support structure with flanges on both ends. This

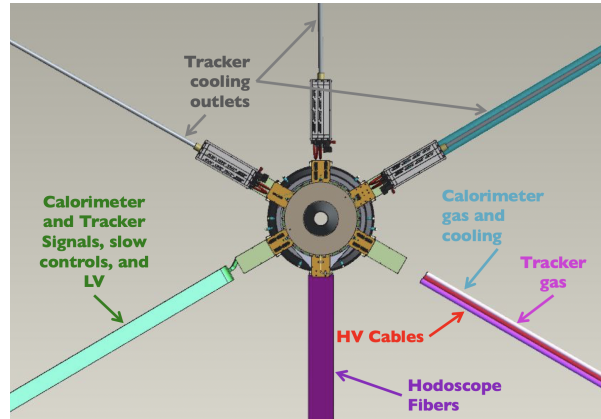


Figure 14: Front view of the Forward Tagger with the routing of cables and services along the CLAS12 torus coils.

669 is needed both for the mounting sequence constraints
 670 and to avoid massive supports in front of the DCs. The
 671 support structure consists of two concentric stainless-
 672 steel pipes connected by adjustment screws to allow for
 673 precise alignment and positioning of the detector with
 674 respect to the beamline and the target position. A third
 675 tungsten cylinder of smaller diameter is located inside
 676 the steel pipes to provide shielding from beam back-
 677 ground.

678 The FT is attached to the support structure via an in-
 679 ner tungsten pipe that is part of the calorimeter assembly
 680 and is located inside the central bore of the FT detec-
 681 tors. This pipe is designed to support the entire weight
 682 of the FT detectors and the additional shielding that is
 683 mounted upstream of the FT. Tungsten was chosen as
 684 the material because, even if less resilient, is more rigid
 685 than stainless steel, thus reducing the gravitational sag-
 686 ging, and has higher density and atomic number, i.e.
 687 better shielding properties. The FT-Cal is kept in po-
 688 sition with respect to the inner tungsten pipe via four
 689 radial supports, made of PEEK. PEEK was chosen be-
 690 cause of its low thermal conductivity (0.25 W/mK) and
 691 its relatively high tensile strength (~ 100 MPa). In ad-
 692 dition, it features high radiation hardness and excellent
 693 stability over a broad range of temperatures. Mounting
 694 rings of PEEK and aluminum, respectively, are used to
 695 support and align the FT-Hodo and FT-Trk on the inner
 696 tungsten pipe.

697 Upstream of the FT, a tungsten cone is attached to
 698 the inner tungsten pipe to provide shielding from Møller
 699 electrons produced by the interaction of the beam in the
 700 target [16]. Figure 2 shows a section of CLAS12 with
 701 the FT in its operating position.

3.2. Routing of Cabling and Services

All services and cables necessary for the operation of the FT detectors are routed along the torus coils to minimize the interference with the CLAS12 Forward Detector as shown in Fig. 14. These include cables for signals, HV, LV, and slow controls, as well as piping for gas distribution and cooling of the three FT subsystems.

The cables and piping are routed along the direction of the magnet coils using appropriate rails. The width and depth of the rails was chosen to be compatible with the space occupied by the DCs (both during normal operation and maintenance) and the clearance between the HTCC and the CLAS12 Forward Detector.

4. FT Prototypes

Two prototypes of the FT-Cal, with 9 and 16 channels, respectively, were designed, assembled, and tested with cosmic rays and electron beams to optimize and validate the detector design. Specifically, the prototypes were used to check the single crystal mechanical assembly, the thermal performance, the front-end and read-out electronics, and the electrical connections via a motherboard. The response to cosmic rays was studied for both prototypes, while the response to electromagnetic showers was studied at Jefferson Lab (JLab) and the INFN Laboratori Nazionali di Frascati (LNF) in Italy. The 9-channel prototype (Proto-9) was tested at JLab using 2-3 GeV electrons deflected by the Hall B tagger system [16], while the 16-channel prototype (Proto-16) was tested at the Beam Test Facility of LNF with a 0.5 GeV electron beam. Extensive simulations were performed and compared to the results of the two sets of measurements. The main goals of the tests were:

- to measure the energy resolution as a function of the single-crystal threshold;
- to measure the energy resolution as a function of T (+18°C, 0°C, -10°C, -25°C);
- to measure the time resolution;
- to verify the system linearity;
- to check rate performance;
- to validate Monte Carlo (GEMC) [17] simulations;
- to measure the electronic noise in realistic conditions;
- to perform detailed studies of the electromagnetic shower signal: shower profile, APD signal shape, and test the filtering algorithm.

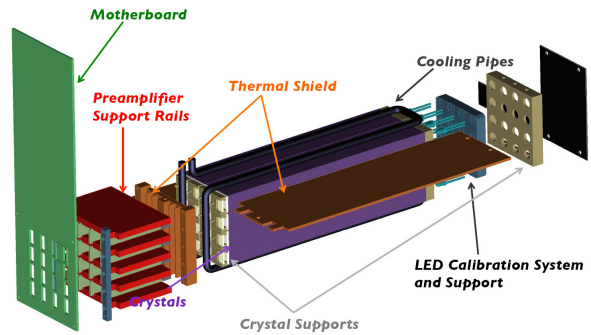


Figure 15: Exploded view of the Proto-16 assembly. From left to right, the CAD drawing shows the motherboard, the system of copper rails holding the preamplifiers, the copper shield back plate, the crystal assembly, the copper shield front plate, and the LED board.

The FT-Cal Proto-16 was built assembling 16 PbWO_4 Type-II crystals in a 4×4 matrix (8 provided by the BTCP and 8 from the RIINC company). Figure 15 shows the Proto-16 components. Many mechanical and electrical solutions tested on Proto-16 were then adopted in the final FT-Cal design. Due to the significant size of the crystal matrix, the expected performance of Proto-16 in terms of energy resolution for showers generated at the center of the 4×4 matrix is similar to what was expected for the FT-Cal. Proto-16 was tested at the Beam Test Facility (BTF) [18] of LNF, using a 0.5 GeV electron beam. Data were taken in October 2012 to study the prototype resolution as a function of the energy deposition and the calorimeter temperature. The BTF electron beam is characterized by a repetition frequency of 50 Hz and a pulse duration of 10 ns. The beam intensity can be varied by operating different sets of slits, selecting the number of electrons per bunch at the level of a single particle. The prototype performance could therefore be studied as a function of the number of electrons simultaneously hitting the crystal matrix, i.e. of the detected energy.

Figure 16 shows the BTF experimental hall after the installation of Proto-16 and the associated equipment. The detector was placed on a movable table that could be displaced in the x and y directions (transverse plane) with a 0.1-mm accuracy. This feature was exploited to center the calorimeter with respect to the beam. A plastic scintillator bar, read out by two PMTs, was placed in front of the beam pipe exit window and was used to determine the arrival time of the electron within the 10-ns bunch duration. The data acquisition system, based on the JLab CODA standard [3], was triggered by the radio-frequency (RF) signal of the Frascati accelerator. For each trigger all of the signals of the Proto-16 crystal



Figure 16: Experimental setup of the Proto-16 test at the LNF Beam Test Facility (BTF). The beam comes from the right. On the left, the detector inside its case (black) is placed on a movable table to allow for centering of the calorimeter with respect to the beam. In front of the calorimeter, a plastic scintillator bar wrapped in black Tedlar is used to determine the arrival time of the beam electrons.

matrix and of the scintillator-bar PMTs were recorded by CAEN VME boards. Both the Proto-16 and scintillator signals were sent to a passive splitter whose two outputs were connected to the 250 MHz FADCs and to leading-edge discriminators. The discriminator output was sent to pipeline TDCs. The samples recorded by the FADCs in an 800 ns window were recorded for each trigger and analyzed offline to evaluate the charge and time.

The conversion between charge and energy was first determined using cosmic ray measurements and then optimized by studying the response of each crystal to 0.5 GeV electrons at the LNF-BTF. It is worth noting that the new calibration constants were found to be within 5-10% of the initial values determined during cosmic-ray data taking. The total reconstructed energy after the full calibration is shown in Fig. 17 for an electron multiplicity on the order of 1-2. The peaks corresponding to different bunch populations are clearly visible and well separated.

Energy Resolution. The mean values and widths (σ) of the peaks in the total reconstructed energy spectrum were analyzed to check the system linearity and to determine the resolution. The measurements were performed by centering the beam on the calorimeter to have the maximum containment of the electromagnetic shower. Figure 18 shows the fitted peak position as a function of total energy in the beam bunch for an APD gain of 150 and a PbWO_4 temperature of 18°C. The linear regression of the experimental points shows no deviations

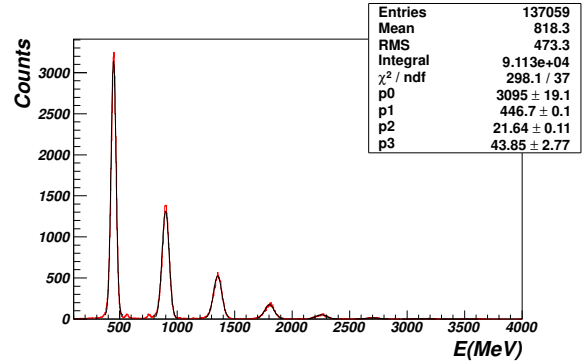


Figure 17: The total energy measured by Proto-16 after calibration. The peaks correspond to different bunch populations and are clearly visible and well separated.

from linearity in the explored range. The same measurement performed in different experimental configurations gave consistent results, confirming that the system is linear up to the maximum measured energy of 4 GeV.

Figure 19 shows the energy resolution as a function of the energy in the beam bunch. The colored points correspond to the resolution measured with Proto-16, while the black open circles are the results of the Monte Carlo (GEMC) simulations. The error bars in the graph show the statistical uncertainty, while the systematic uncertainty was estimated to be on the order of 5%. As expected, the experimental resolution improves for increasing energy, reaching an asymptotic behavior at about 3 GeV. The measurements performed in different configurations are in general consistent, varying within a range of 0.5% except for the resolution obtained at room temperature and $G=75$ (orange points). The resolution in this case is systematically worse than that obtained at the same temperature but $G=150$. This was interpreted as due to the preamplifier noise being the dominant factor in determining the resolution at this temperature. From this we concluded that working at higher APD gain is the preferable configuration.

The comparison of the resolutions obtained at different temperatures shows that lower temperatures, corresponding to higher light yield, and therefore a larger signal, give a better resolution. The best values were obtained at -20°C , where the experimental points are in good agreement with the simulation results. The dependence of the resolution on the temperature is more evident for high bunch energies, where threshold effects are smaller. Above 2 GeV, the resolution at room temperature seems to be systematically higher than that obtained at 0°C or -20°C with a difference of about 0.5%. The difference of the resolution obtained at 0°C and -20°C

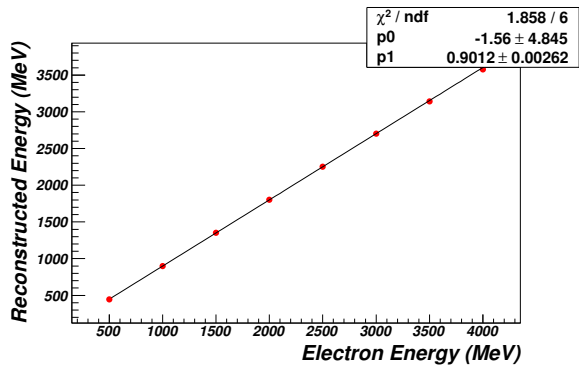


Figure 18: Proto-16 reconstructed energy as a function of the beam bunch energy. The red points were obtained at room temperature and with an APD gain of 150. The linear regression of the experimental points shows no deviation from linearity.

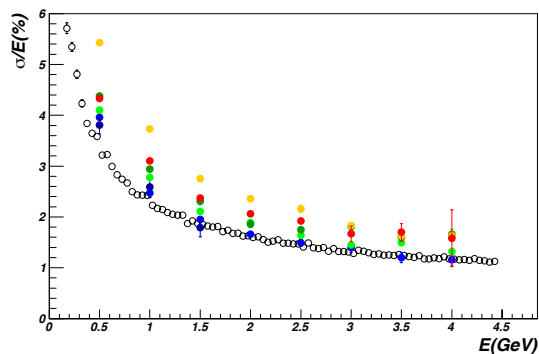


Figure 19: Proto-16 energy resolution as a function of the beam bunch energy. The red and orange points were obtained at room temperature for APD gains of 150 and 75, respectively. The green points correspond to 0°C ; the darker points were obtained removing the passive splitter. The blue and dark-blue points, that partially overlap, correspond to -20°C with APD gains of 150 and 75, respectively. The open black circles show the expected resolution based on Monte Carlo simulations. Only statistical uncertainties are shown.

is on the contrary negligible within the systematic uncertainties. Based on these results and considering the technical difficulties in operating the FT-Cal at the lowest temperature, we chose the optimal operating temperature of the calorimeter to be 0°C .

5. Detector Simulations

Detailed simulations of the FT have been done with the Geant4-based Monte Carlo code for CLAS12, GEMC [17], to optimize the detector design, to develop the reconstruction algorithms, and to understand the detector performance.

Details on the implementation of the FT in GEMC of the detector geometry and digitization are reported in

Ref. [17], while an extensive discussion of the simulation studies that guided the detector design are presented in Ref. [14]. Here we focus on summarizing the results of the simulation studies that are relevant to understand the FT performance.

5.1. Leakage Corrections

The reconstructed cluster energy can be systematically smaller than the actual energy of the particle that induced the shower due to leakages in the shower containment caused by the limited dimensions of the calorimeter, by cuts in the clustering algorithms, and by the thresholds in the hit detection. An example of the difference between the reconstructed cluster energy and the simulated electron energy is shown in the top panel of Fig. 20. This was obtained assuming an equivalent threshold on the individual crystals of 10 MeV: the leakage varies from ~ 80 MeV (16%) for 500 MeV electrons to ~ 300 MeV (6.6%) for 4.5 GeV electrons.

This effect can be easily corrected for by parameterizing the leakage as a function of the reconstructed cluster energy and position, and applying the correction in reconstruction. Simulations of single electrons were performed in GEMC and the difference between the reconstructed cluster energy and the electron energy was studied as a function of the cluster seed crystal (i.e. the crystal with the largest signal). For each crystal, the dependence of this difference on the reconstructed cluster energy was fit to a fourth-order polynomial, which was then used as an additive correction to the reconstructed cluster energy. The final dependence of the difference between the corrected cluster energy and simulated energy is shown in the bottom panel of Fig. 20.

5.2. Electromagnetic Background and Radiation Dose

The electromagnetic background produced by the interaction of the electron beam in the target at the nominal CLAS12 luminosity was simulated in GEMC. For this purpose, in each event, about 124k, 11-GeV electrons were generated that originated 10 cm upstream of the target. The electrons were distributed randomly with the radio-frequency structure of the beam in a 250-ns window. This number of electrons corresponds to the number of beam electrons that would pass through the target in the chosen time window at the nominal CLAS12 luminosity of $10^{35} \text{ cm}^{-2}\text{s}^{-1}$. These simulations were used to study background rates in each of the FT detectors, to determine the pile-up probability, and to estimate the radiation dose the FT would be subject to during operations.

The overall particle rate in the FT was found to be about 120 MHz, dominated by very low-energy

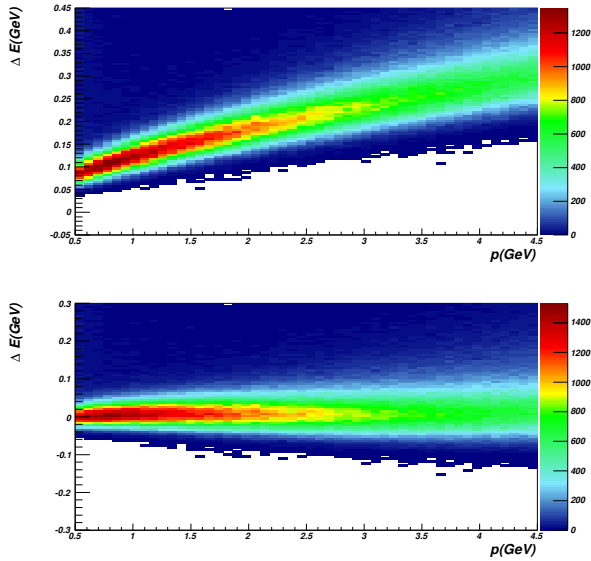


Figure 20: Top: difference between the simulated electron energy and the reconstructed cluster energy as a function of the electron momentum for a 10 MeV equivalent threshold on the single crystal signal. Bottom: difference between the simulated electron energy and the cluster energy after the leakage correction.

particles, with only 6% due to particles with energy above 100 MeV. In the energy range to be tagged (0.5-4.5 GeV) the overall particle rate is further reduced to about 180 kHz, equally shared between photons and hadrons.

For the FT-Cal, the energy deposition in each crystal was evaluated from the background simulation and used to calculate the dose per unit of time. The overall radiation dose at $10^{35} \text{ cm}^{-2} \text{ s}^{-1}$ was estimated to be less than 1.5 rad/hr when averaged over the entire calorimeter with a distribution on the calorimeter crystals as shown in Fig. 21. The maximum dose per crystal is about 3 rad/hr, which would result in a maximum integrated dose per crystal of about 2160 rad in 30 days of beam time.

6. Detector Calibration and Commissioning

6.1. Pre-beam Calibration

Initial checkout and calibration of the FT detectors upon completion of the installation were performed via:

- Pulser, LED, and cosmic ray runs for the FT-Cal;
- Pulser and cosmic ray runs for the FT-Hodo;
- Pulser and pedestal runs for the FT-Trk.

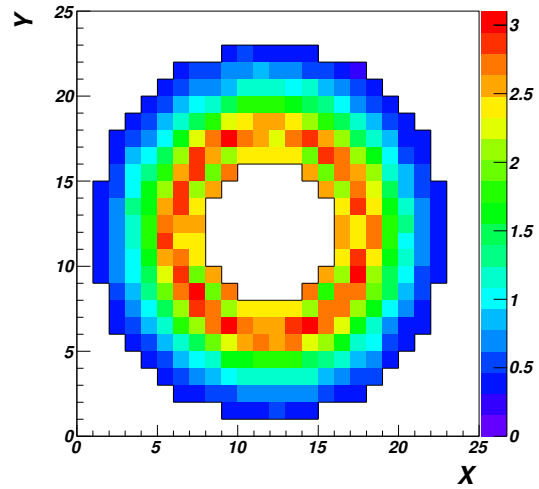


Figure 21: Radiation dose on the FT calorimeter crystals in rad/hr at $10^{35} \text{ cm}^{-2} \text{ s}^{-1}$ luminosity. The maximum values of about 5 rad/hr are observed for the innermost crystals, i.e. at the smaller angles.

6.1.1. FT-Cal Pre-beam Calibration

Initial checkout of the calorimeter was performed via pulser and LED runs. In the pulser runs, an external clock was used to trigger the readout of the entire FT-Cal recording the full FADC waveforms in a 400-ns window in the absence of a physics signal to measure baselines and to monitor noise, for the purpose of identifying disconnected or malfunctioning channels. For each crystal, several parameters were studied, such as the average pedestal, the event-by-event pedestal RMS, and the noise defined as the sample-by-sample pedestal RMS. The analysis was performed online, connecting to the data acquisition Event Transfer (ET) ring [3], or from a recorded data file using the FT Java calibration suite [19]. Figure 22 shows a view of a typical pulser run analysis. One of the most useful results obtained from this analysis is the average channel noise that is indicative of its functionality: a noise level below the typical range is indicative of a malfunctioning preamplifier or a disconnected cable, while a noise level above the typical range can indicate a high-voltage issue since the noise introduced by the LAAPDs is higher when the biased voltage is not applied.

Once the initial debugging of the system based on pulser runs was completed, a second checkout based on LED runs was performed. In this case, the FT-Cal LMS was used to input light into each of the calorimeter crystals and the corresponding signals were recorded to check the pulse amplitude and shape, and to assess the correct functioning of the LAAPDs, preamplifiers,

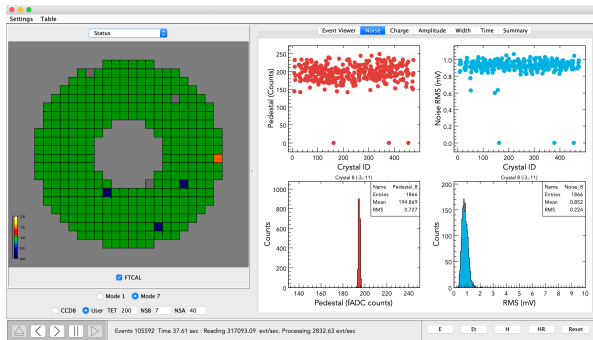


Figure 22: Results of the FT-Cal noise analysis from a pulser run. The left part of the calibration suite display shows a view of the calorimeter with a color scheme representing the status of the crystal: green corresponds to a fully functional element, blue to an element with noise below the typical range (indicative of a low-gain preamplifier), orange to an element with noise above the typical range, and gray to a crystal for which no data were recorded. The right part of the panel shows the average pedestal and noise as a function of the crystal number, and the event distribution of the pedestal and noise for the selected crystal.

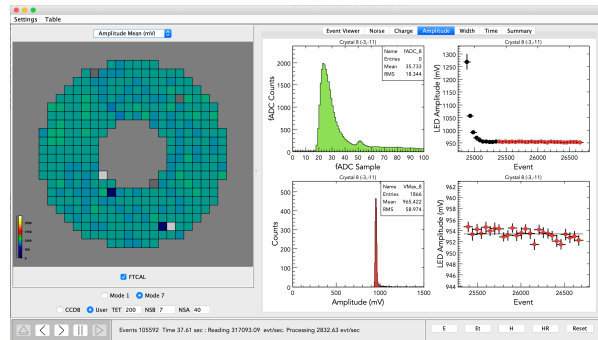


Figure 23: Results of a typical FT-Cal LED run. The left part of the calibration suite display shows a view of the calorimeter with a color scheme representing the LED pulse amplitude. The right part of the panel shows for the selected crystal the average pulse shape (top left), the pulse amplitude as a function of the event number, i.e. of time (top right), the distribution of the amplitudes (bottom left), and the pulse amplitude as a function of the event number after the LED has reached stability (bottom right). The latter is fit to a constant to determine the pulse amplitude that is displayed in the detector view.

962 and front-end electronics. Using the EPICS slow controls 991
 963 interface of the LMS, the LEDs can be switched 992
 964 on in groups of 6, one per driver, in a predefined 993
 965 sequence and pulsed at a rate of 62.5 Hz for a time 994
 966 interval of 30 s to accumulate about 1800 waveforms 995
 967 per channel. The LED pulse amplitudes have been tuned 996
 968 to provide a maximum amplitude at the FADC of about 997
 969 1 V, which is representative of a typical signal expected 998
 970 for the calorimeter. The recorded waveforms are analyzed 999
 971 to extract the pulse amplitude as a function of 1000
 972 time. In fact, upon being turned on, the LED light 1001
 973 intensity undergoes an exponential drop until it reaches 1002
 974 stability. This typically happens within 6-8 s. The amplitude 1003
 975 in the stability region is fit to a constant to extract 1004
 976 the average value that is recorded and compared to 1005
 977 reference values to detect changes in the detector response 1006
 978 and potential failures. Figure 23 shows the results of the 1007
 979 analysis of a typical LED run as displayed by the 1008
 980 calibration suite. In this specific case, the analysis shows a 1009
 981 relatively uniform response to the LED light, with typical 1010
 982 amplitudes on the order of 1 V as defined by the 1011
 983 design, with a few problematic channels that coincide 1012
 984 with those identified by the pulser runs of Fig. 22. 1013
 985 The final calibration of the FT before in-beam test- 1014
 986 ing was based on the study of the detector response to 1015
 987 cosmic rays. A special FPGA-based trigger was developed 1016
 988 by the JLab Fast Electronics Group to select events 1017
 989 where a cosmic ray crosses the calorimeter primarily in 1018
 990 the vertical direction, i.e. crossing the crystals along 1019

the short side. This is achieved by requiring a minimum 992
 number of signals above threshold in the crystals 993
 that are in a “column” of the calorimeter assembly, 994
 a technique that exploits the functionalities of the 995
 JLab FADCs and trigger electronics [3, 20]. For these 996
 events, the waveforms for all crystals in the calorimeter 997
 were recorded and analyzed offline using the FT-Cal 998
 calibration suite. Details of the analysis procedure are 999
 reported in Refs. [21, 22]; here we summarize only the 1000
 main steps and results. For each crystal, events where at 1001
 least N_{min} crystals with signal above threshold are found 1002
 in a vertical range of N_{range} crystals above or below the 1003
 chosen one were selected. After optimization, the values 1004
 of N_{min} and N_{range} were fixed to 4 and 5, respectively. 1005
 For these events, the crystal waveform was integrated 1006
 in a fixed range and pedestal subtracted to extract the 1007
 charge. The integration range was optimized empirically 1008
 to maximize the signal-to-noise ratio. The charge distribution 1009
 for all selected events in the given crystal was then fit 1010
 with a Landau summed with an exponential function, representing 1011
 the minimum-ionizing particle (MIP) deposition and background, 1012
 respectively. The mean of the Landau function, compared with the 1013
 expected average energy deposition determined from 1014
 Geant4 Monte Carlo simulations to be 15.3 MeV, was then 1015
 used to evaluate the charge-to-energy conversion factor for 1016
 each crystal.

Figure 24 shows an example of a cosmic ray event 1017
 as displayed by the calibration suite and an example of

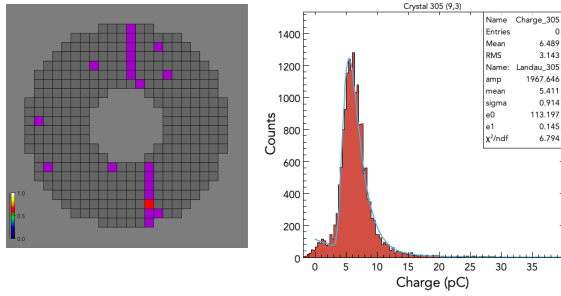


Figure 24: Left: example of a cosmic ray crossing the calorimeter vertically as displayed by the calibration suite. Right: example of the measured charge distribution measured from the selected events for a calorimeter crystal; the blue line shows the results of the Landau plus exponential fit; the mean of the Landau function is used to estimate the charge-to-energy conversion factors.

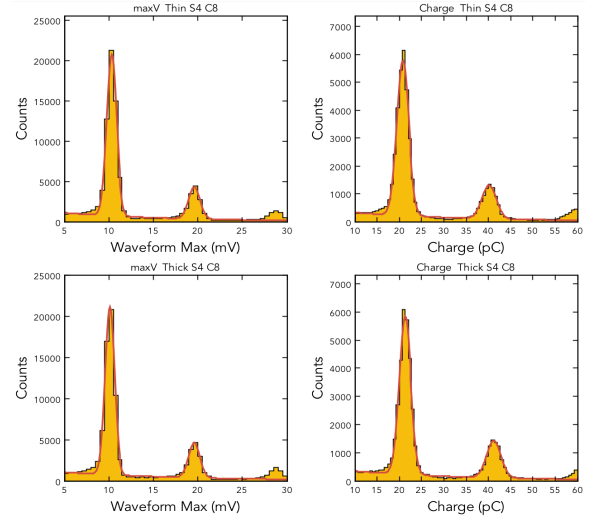


Figure 25: SPE signal from the FT-Hodo SiPMs reading signals from the thin (top) and thick (bottom) tiles, in mV (left) and pC (right), determined using the waveform maximum and integral, respectively.

1020 the charge distribution for a selected crystal obtained by
 1021 integrating over the selected events. The typical values
 1022 of the Landau peak were found to be in the range of
 1023 4-7 pC at the calorimeter operating temperature of 0°C
 1024 and the corresponding conversion factors in the range 1053
 1025 of 2.2-3.8 MeV/pC. These values were used as the cal- 1054
 1026 ibration constants for the initial reconstruction of beam 1055
 1027 data, although it was found that these constants usually 1056
 1028 led to an overestimate of 20% of the actual energy de- 1057
 1029 posited in the energy range of interest for the calorime- 1058
 1030 ter of 0.5-4.5 GeV. While this discrepancy is significant, 1059
 1031 it is not unexpected given the uncertainties in extract- 1060
 1032 ing the cosmic ray signal from the background and the 1061
 1033 large difference in the two calibration points, since cos- 1062
 1034 mic rays deposit an energy in the range of tens of MeV, 1063
 1035 while the energy range for beam-induced signals is two 1064
 1036 orders of magnitude larger. 1065

1037 6.1.2. FT-Hodo Pre-beam Calibration 1067

1038 Similarly to the calorimeter, initial checkout of the 1068
 1039 hodoscope was performed via pulser runs to check the 1069
 1040 functionality of each electronics channel and to evalu- 1070
 1041 ate the SiPM gains by measuring the single photoelec- 1071
 1042 tron (SPE) signal. An external clock was used to trigger 1072
 1043 the data acquisition, which recorded the waveform of all 1073
 1044 232 channels in a 400 ns window. The waveforms could 1074
 1045 be analyzed online by connecting the calibration suite to 1075
 1046 the data acquisition ET ring [3] or offline reading from 1076
 1047 the data file. The parameters that were monitored are the 1077
 1048 pedestal values, the pedestal RMS, and the electronic 1078
 1049 noise. The extracted SPE values were compared to the 1079
 1050 typical ones to identify problematic channels and dis- 1080
 1051 connected cables. For each channel, the waveforms that 1081
 1052 exceeded a minimum threshold above the baseline were 1082

analyzed to extract the SPE signal. For this purpose, the waveforms were integrated in a fixed time range and pedestal subtracted. The distribution of the extracted charge for a selected channel is shown in Fig. 25, where the top and bottom plots are for the same tile in the two detector layers and the left and right plots show the results obtained using the waveform maximum and integral, respectively. Clear peaks corresponding to one, two, and three photoelectrons are visible; the difference between the peaks was used to determine the gain of the channel, resulting in typical values on the order of 20 pC/phe. The consistency of the results obtained using the pulse maximum and integral confirms the reliability of the waveform analysis.

Further checkout of the detector was performed via cosmic ray data taking. The same FPGA-based trigger developed for the calorimeter was used to trigger the data acquisition system on events in which multiple tiles of the hodoscope had a signal above threshold. For such events, all hodoscope channel waveforms were recorded and analyzed offline. The signal charge was extracted by integrating the waveform in a fixed time window and subtracting the pedestals. The resulting charge distributions were inspected to ensure a sizable signal for all tiles. In this case no attempt was made to extract the charge-to-energy conversion factor from these distributions because of the unfavorable orientation of the hodoscope in the installation position for the measurement of cosmic rays that could cross the scintillation tiles with a very large angular and energy deposi-

1083 tion spread.

1084 6.1.3. FT-Trk Pre-beam Calibration

1085 The first calibrations and tests of the trackers were
 1086 performed using the cosmic-ray test bench available at
 1087 CEA-Saclay [15]. The goal of these tests was to opti-
 1088 mize the operating conditions of the detectors and to
 1089 compute their two-dimensional efficiency maps using
 1090 cosmic muons prior to shipment to JLab. Figure 26
 1091 shows the results for two of the four detector layers, in-
 1092 dicated a good uniformity of the response over the full
 1093 active area.

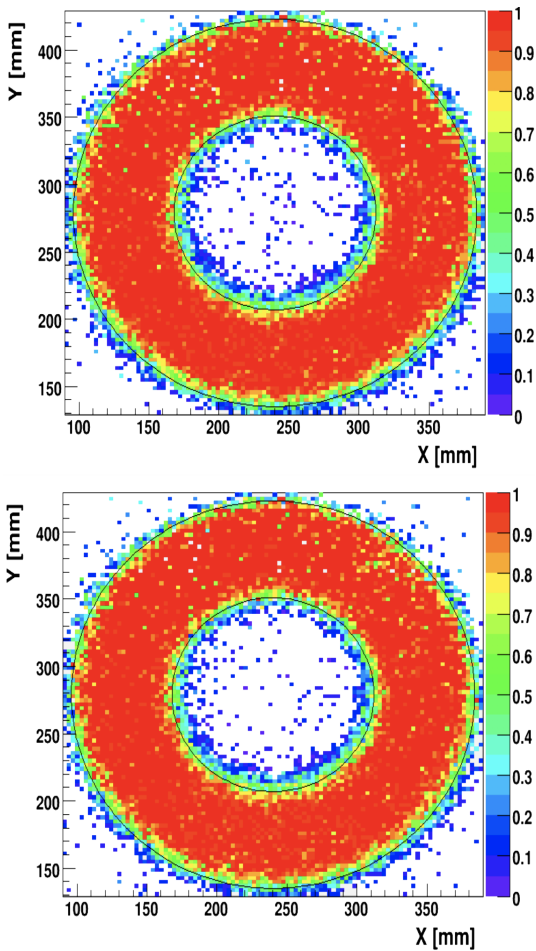


Figure 26: Two-dimensional (y vs. x coordinate) efficiency map for the two layers of one of the FT tracker detectors as measured in the cosmic-ray setup at CEA-Saclay. The black circles indicate the limits of the detector active area.

1094 After installation, the initial checkout of the FT-Trk
 1095 and, in particular, of the front-end electronics, was per-
 1096 formed by means of pedestal and pulser runs. Since

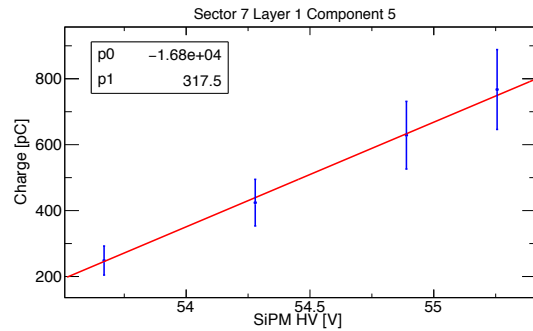


Figure 27: Dependence of the MIP mean position on the SiPM bias voltage for a single hodoscope tile. The dependence is fit to a linear function that is used to select the operating voltage to give an average MIP signal close to the chosen value.

1097 these procedures are standard for the CLAS12 Mi-
 1098 cromegas detectors, we refer to Ref. [15] for further de-
 1099 tails.

1100 6.2. In-beam Calibration and Commissioning

1101 While pre-beam calibrations were essential to ensure
 1102 all detector components were fully operational, the final
 1103 calibrations to extract the parameters needed for the FT
 1104 reconstruction are based on analysis of beam data. Here
 1105 we report specifically on the procedures developed for the
 1106 calibration of the calorimeter and hodoscope, since
 1107 no specific calibrations are needed for the tracker.

1108 For both the hodoscope and calorimeter, energy and
 1109 time calibrations can be obtained from the analysis of
 1110 data recorded with the CLAS12 production triggers and
 1111 do not require dedicated data taking. A dedicated run
 1112 is typically employed, however, for matching the gains
 1113 from all FT-Hodo SiPMs [6]. In this dedicated run, av-
 1114 erage minimum-ionizing particle signals were obtained
 1115 for a set of different HV settings (see Fig. 27), deter-
 1116 mining the slope and intercept from which gain matching
 1117 is established.

1118 The energy calibration for the FT-Cal is achieved by
 1119 analyzing electron elastic scattering events or by recon-
 1120 structing the $\pi^0 \rightarrow \gamma\gamma$ decay where both photons are
 1121 detected in the calorimeter.

1122 Elastic $ep \rightarrow ep$ scattering data were found to be
 1123 particularly effective for calibrations at low beam en-
 1124 ergy. Data using a 2.2 GeV beam were collected dur-
 1125 ing the CLAS12 engineering run. Events with only one
 1126 cluster in the FT-Cal were selected (from the scattered

⁶Having a matched gain from all FT-Hodo SiPMs allows for a common trigger readout threshold for all channels.

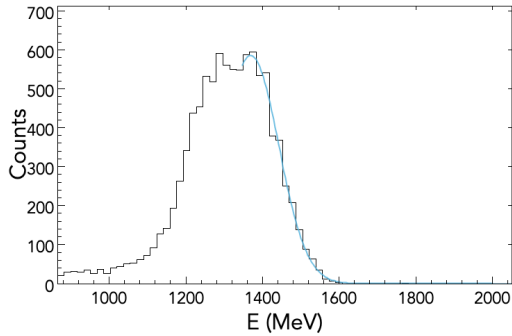


Figure 28: Example of the seed energy distribution for a selected crystal for elastic events at 2.2 GeV beam energy. The blue line shows the fit used to determine the edge of the distribution.

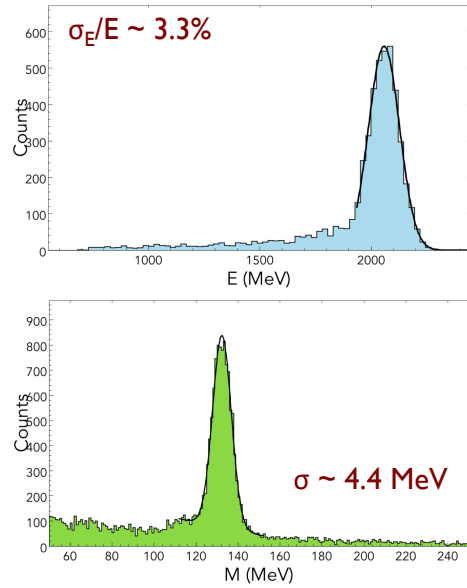


Figure 29: Top: electron energy spectrum reconstructed at 2.2 GeV beam energy in the FT-Cal; the peak corresponds to elastic scattering; after calibrations based on elastic events, an overall energy resolution of 3.3% at 2.2 GeV is found. Bottom: $\pi^0 \rightarrow \gamma\gamma$ invariant mass spectrum reconstructed at 10.6 GeV beam energy using the elastic scattering energy calibrations: the width of the π^0 peak determined via a Gaussian fit was found to be ~ 4.4 MeV.

electron) and, based on the existing cosmic ray calibrations, the energy of the crystal with the largest signal, i.e. the *seed*, was extracted. For each crystal, these events were accumulated requesting the seed energy to be larger than 55% of the total cluster energy. The right edge of the distribution of the seed energy was fit with a Gaussian function to extract the peak position. The mean value of the Gaussian function was compared to that expected based on Geant4 Monte Carlo simulations to extract a correction to the charge-to-energy conversion factor used in the cluster reconstruction. Figure 28 shows an example of the seed energy distribution and the cluster energy distribution for a selected crystal. Using these constants, an energy resolution of 3.3% at 2.2 GeV beam energy was determined by fitting the reconstructed elastic peak (see Fig. 29). This resolution is about 1% larger than what is expected from simulations as discussed in Section 8. With the same calibration constants, the $\pi^0 \rightarrow \gamma\gamma$ decay was reconstructed at 10.6 GeV beam energy selecting events with both photons detected in the FT-Cal, finding the width of the π^0 peak to be ~ 4.4 MeV, which gives an energy resolution of $\sim 3.2\%$.

Since the effectiveness of the elastic calibration is limited to beam energies on the order of a few GeV because of the rapid decrease of the corresponding cross section at higher energies, an alternative approach was developed to perform the energy calibration of the FT-Cal based on $\pi^0 \rightarrow \gamma\gamma$ decays. Events where both photons are detected in the calorimeter were selected and filtered applying the following cuts:

- the energy of both clusters, as reconstructed based on existing calibrations, is larger than 500 MeV;
- the size of both clusters, i.e. the number of crystals involved, is larger than 3;

- the opening angle between the two clusters is larger than 2° .

The last cuts are useful to reduce backgrounds resulting from split clusters, i.e. events in which a secondary particle originating from the electromagnetic shower creates a second cluster at a close distance to the primary cluster. For each crystal, events in which the crystal is the seed of one of the two clusters are accumulated and the ratio between 1) the measured cluster energy for the given crystal and the energy calculated from the nominal π^0 mass and 2) the other cluster energy is computed. The distribution of such ratios is fit with a Gaussian function to derive a correction factor for the charge-to-energy calibration constant of the selected crystal. The procedure is applied iteratively until the π^0 mass spectrum for all crystal is within 0.5 MeV of the nominal value.

Figure 30 shows an example of the ratio distribution and of the π^0 mass spectrum for a selected crystal before and after (blue histogram) the calibration procedure. The advantage of this procedure is that it does not strongly depend on the beam energy and exploits the full energy spectrum of the clusters, providing a check of the linearity. The left panel of Fig. 31 shows the correlation between the measured and computed cluster energies af-

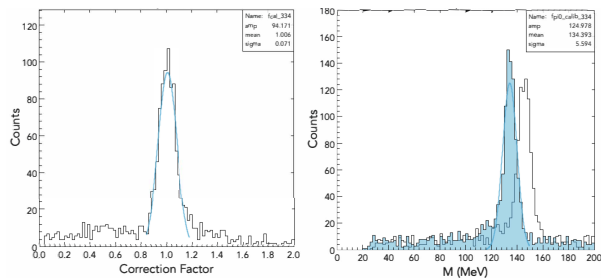


Figure 30: Left: calibration correction factor for a selected crystal computed as the ratio between 1) the measured energy of clusters where the crystal is the seed and the energy calculated from the nominal π^0 mass and 2) the other cluster energy. Right: π^0 mass spectrum for the same crystal before (unfilled histogram) and after (filled histogram) the calibration procedure.

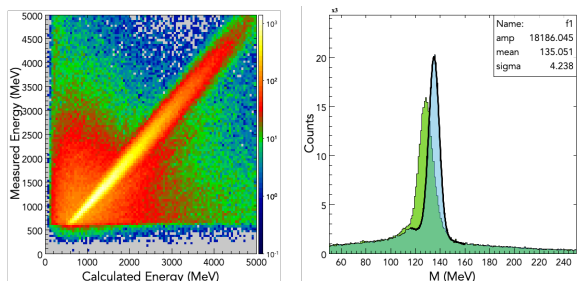


Figure 31: Left: correlation between the measured cluster energy and the energy computed from the nominal π^0 mass; the range covered is well matched to the FT energy range of interest. Right: π^0 mass spectrum before (green) and after (blue) the calibration; the achieved resolution is ~ 4.2 MeV.

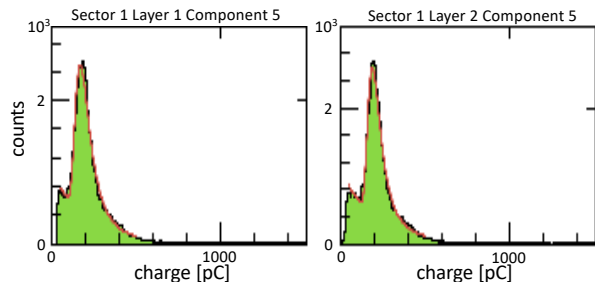


Figure 32: Signals from two FT-Hodo tiles (thin and thick layer) fit with a Landau plus an exponential to established the charge-to-energy constants.

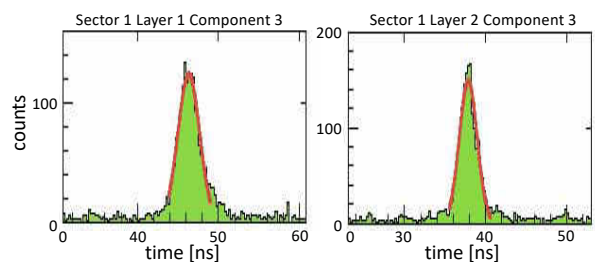


Figure 33: FT-Hodo time corrections determined by Gaussian fits on the time difference between the hit time projected back to the event vertex and the event start time for a thin (left) and thick (right) tile.

1187 ter calibration: the energy range, which is covered with 1213
 1188 good statistics, is from 0.5 to 5 GeV with a perfect over- 1214
 1189 lap with the energy range of interest for the CLAS12 1215
 1190 experimental program with the FT. The resolution that 1216
 1191 is achieved with this calibration algorithm is of the order 1217
 1192 of 4-5 MeV integrated over the entire calorimeter as 1218
 1193 shown by the right panel of Fig. 31 1219

1194 The energy calibration of the FT-Hodo is performed 1220
 1195 by studying the energy deposition of MIPs, since these 1221
 1196 are the typical signals expected from charged particles 1222
 1197 impinging on the detector. Figure 32 shows the charge 1223
 1198 from MIP signals in the thin and thick tiles. For the FT- 1224
 1199 Hodo, charged particle signals are selected by requiring 1225
 1200 the geometrical matching of tiles in the two layers. No 1226
 1201 other requirement or matching with other detectors is 1227
 1202 requested to minimize the dependency on other system 1228
 1203 calibrations. The distributions are fit with a Landau 1229
 1204 plus an exponential function to determine the average MIP 1230
 1205 charge. The charge-to-energy conversion factors are deter- 1231
 1206 mined by comparing the resulting values to the ones 1232
 1207 estimated from Geant4 Monte Carlo simulations. The 1233

constant values were found to be very stable with time, 1208
 requiring the calibration to be performed only at the be- 1209
 ginning of a new data taking period or after a change of 1210
 the detector operating conditions (e.g. a change of the 1211
 HV settings). 1212

The timing calibrations of both the FT-Cal and FT- 1213
 Hodo are obtained by studying the time correlation of 1214
 the signals in the two detectors with the CLAS12 For- 1215
 ward Time-of-Flight (FTOF) detector [23]. The proce- 1216
 dure makes use of events with a scattered electron in 1217
 the CLAS12 Forward Detector and a second particle de- 1218
 tected in the FT. In such events, the start time t_0 , i.e. the 1219
 time of the interaction of the beam electron in the target, 1220
 can be computed from the electron FTOF time projected 1221
 back to the event vertex. The start time can then be used 1222
 as a reference for the calibration of the FT detectors. 1223

For the FT-Hodo, the signal time, t_{hit} , projected 1224
 back to the event vertex is compared to the event start 1225
 time, t_0 . The difference between the two times gives the 1226
 time correction needed. Figure 33 shows an example of 1227
 the time offset distribution for a thin and a thick tile. 1228

The same procedure is used for the FT-Cal, however, 1229
 all hits with energy greater than 10 MeV are used with 1230
 no requirement on the charge of the associated particle. 1231
 The use of such a low energy threshold is important to 1232
 be able to calibrate the crystals that are on the edges of 1233

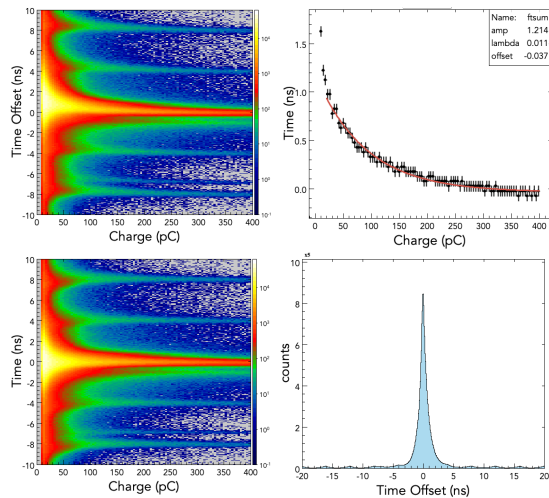


Figure 34: Top: FT-Cal time offset dependence on the charge (left); the profile of the histogram is fit to a power law, a/q^λ . Bottom: FT-Cal time offsets after the time-walk correction and the subtraction of the residual constant term.

the calorimeter. The measured time is then compared with the event start time, extracting both an overall offset and a charge-dependent correction, associated with a time-walk effect. The top-left panel of Fig. 34 shows the time offset as a function of the signal charge; this histogram profile is fit to a power law, a/q^λ , as shown in the top-right panel to determine the time-walk correction. After applying this correction, the time offset distribution shown in the bottom plots of the same figure are fit to a simple Gaussian function to determine the global offset. The bottom right plot shows the final distribution with all corrections, showing a clear coincidence peak at 0 surrounded by the accidental peaks at multiples of ± 4.008 ns due to the RF beam structure. The time offset constant term is extracted for each crystal separately, while the time-walk constants are fit for all crystals together since no significant difference between the crystals was found. The resolution achieved with this procedure is reported in Section 8.

7. Event Reconstruction

Reconstruction of the FT sub-detector information and the matching between the detectors to determine the type and three-momentum of the incident particles is implemented in the CLAS12 Java reconstruction framework. Details on the algorithms and implementation are provided in Ref. [19]. In the following we briefly summarize the main steps and final outputs.

FT-Cal hits are reconstructed from the analysis of

the recorded FADC information to extract energy and time; hits are then associated based on position and time to form clusters whose energy and centroid position are used as an initial seed to define the three-momentum of the incident particles. Similarly, FT-Hodo hits are reconstructed from the FADC raw information and matched based on position and timing to form clusters of matching tiles in the two layers of the detector. These are matched to clusters in the calorimeter based on position and time to distinguish charged particles from neutrals. Finally, FT-Trk hits are also reconstructed from the raw data and geometrically grouped to form clusters in each of the detector layers separately. Combinations of clusters in the $x - y$ layers of each of the two sub-detectors are used to define crosses that are finally matched to calorimeter clusters to improve the determination of the impact point of the particle.

8. Detector Performance

Data at different beam energies and with different trigger conditions have been analyzed to study and assess the FT performance. Results from the studies are detailed below.

8.1. Acceptance

The detector acceptance was studied in detail at the maximum beam energy the experiment operated at so far of 10.6 GeV. Data were recorded with a minimum-bias trigger based on the FT-Cal alone with a threshold on the measured cluster energy of 100 MeV. In the offline analysis, events were further selected, requiring a reconstructed electron via the matching of the FT-Cal cluster to FT-Hodo hits, and the associated FT-Cal cluster to have total energy greater than 500 MeV, seed energy greater than 300 MeV, and size greater than or equal to 4 crystals. The resulting event distributions as a function of the electron energy and polar angle are shown in Fig. 35.

The energy coverage extends from 500 MeV, as selected in the offline analysis, up to the end-point set by the beam energy where elastic scattering dominates. Close to the energy end-point, the detector resolution is expected to worsen significantly because of saturation of the FT-Cal preamplifiers and FADCs that are optimized for the design energy range of 0.5-4.5 GeV. The θ range extends from the minimum angle of 2.5° to $\sim 5^\circ$. The two-dimensional distribution shows the effect of the CLAS12 solenoid field on low-momentum electrons starting from $\theta \sim 2^\circ$ that are bent into the detector

1310 acceptance. The detector acceptance matches and partially
 1311 exceeds the design specifications.

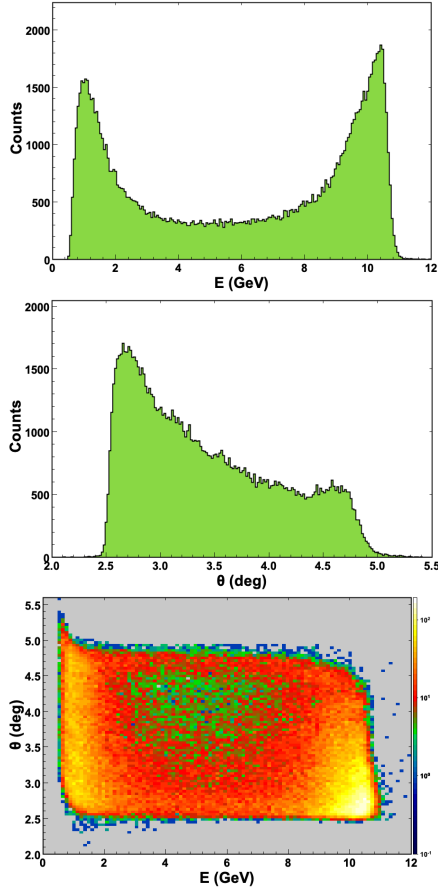


Figure 35: FT acceptance for electrons as a function of energy (top), polar angle (middle), and of both variables (bottom) at 10.6 GeV beam energy. The energy range goes from 500 MeV, as selected in the off-line analysis, up to the end-point set by the beam energy where elastic scattering dominates. The θ range goes from the minimum angle of 2.5° to $\sim 5^\circ$. The two-dimensional distribution shows the effect of the CLAS12 solenoid field on low-momentum electrons that start from $\theta \sim 2^\circ$ and are bent into the detector acceptance.

1312 8.2. Energy Resolution and Electromagnetic Shower 1313 Reconstruction

1314 Within the detector acceptance, the energy resolution
 1315 was studied based on elastic scattering and π^0 decay to
 1316 two photons, as discussed in Section. 6. The results indicate
 1317 the currently achieved resolution is larger than the design
 1318 value by about 1% at 2 GeV. The reasons for this discrepancy
 1319 can be multi-fold. First, the energy calibration of individual
 1320 crystals has shown a significant spread in the energy-to-charge
 1321 conversion that was not foreseen in the initial estimates.
 1322 This spread, likely due to the

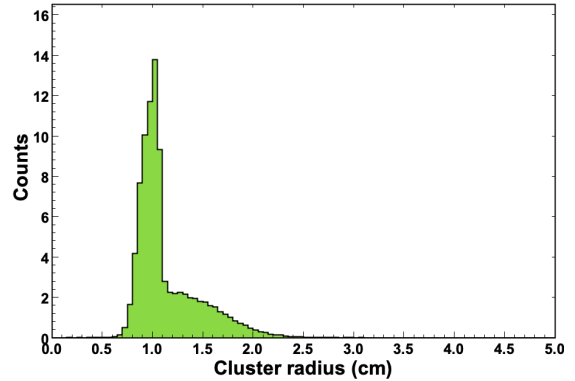


Figure 36: Radius of the FT-Cal shower for charged particles. A clear peak at ~ 1 cm associated with electron-induced electromagnetic showers overlaps with a broader distribution due to hadronic showers.

1323 non-uniformity of the crystal light yield, can contribute
 1324 to a worsening of the resolution because it results in a
 1325 non-homogeneous detector response. Second, as a consequence
 1326 of the crystal non-uniformity, the threshold applied in the
 1327 cluster reconstruction is for some crystals larger than the
 1328 10 MeV used in the simulation studies and prototype analyses.

1330 The shower profile in the FT-Cal was studied and compared
 1331 to Monte Carlo simulations for different particle species. Figure
 1332 36 shows the shower radius, defined as the square root of the
 1333 second moment of the shower, for charged particles, i.e. particles
 1334 associated with a cluster in the calorimeter with matching hits
 1335 in the hodoscope. A clear peak with radius of ~ 1 cm associated
 1336 with electrons is clearly visible, overlapping a broader
 1337 distribution associated with hadronic showers. The shower profile
 1338 and, specifically the cluster radius, can therefore be used to
 1339 discriminate between different particle types.

1343 8.3. Timing Resolution

1344 The timing resolution for electrons and photons was
 1345 evaluated from beam data by correlating the reconstructed
 1346 cluster time from the FT-Cal to either the RF signal that is
 1347 synchronous with the CEBAF accelerator beam bunches or the
 1348 event start time derived from the CLAS12 FTOF system [23].
 1349 Specifically, the electron time resolution was studied correlating
 1350 the FT time projected back to the event vertex to the RF
 1351 signal time. The difference of these two times for 10.6 GeV
 1352 data is shown in Fig. 37 for electrons with energy greater
 1353 than 500 MeV, cluster seed energy greater than 300 MeV, and
 1354 cluster size greater than or equal to 4 crystals: a Gaussian
 1355 fit to the distribution gives $\sigma \sim 140$ ps. The tails of

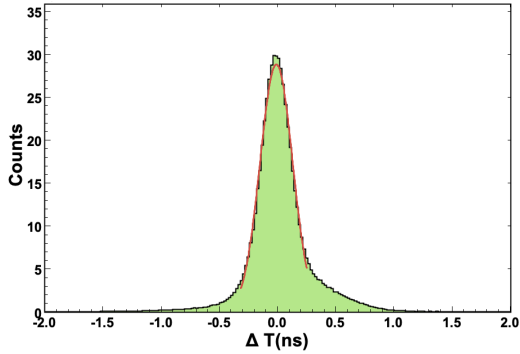


Figure 37: Time resolution for electrons detected in the FT with energy greater than 500 MeV, seed energy greater than 300 MeV, and cluster size greater than or equal to 4. The histogram shows the time difference between the FT time projected back to the event vertex and the RF signal time. The Gaussian fit gives a resolution $\sigma \sim 140$ ps.

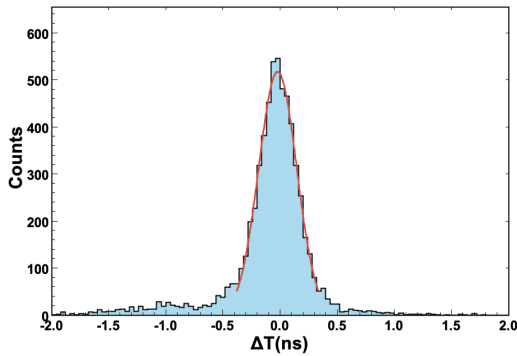


Figure 38: Time resolution for photons detected in the FT with energy greater than 500 MeV, seed energy greater than 300 MeV, and cluster size greater than or equal to 4. The histogram shows the time difference between the FT time projected back to the event vertex and the event start time derived from the CLAS12 FTOF detector for events where an electron is identified in the CLAS12 Forward Detector. The Gaussian fit gives a resolution $\sigma \sim 150$ ps.

the distribution are due to low-energy clusters close to the applied selection threshold, and are expected to be reduced by improvements of the time-walk correction that are currently under study.

While this estimate of the time resolution relies solely on the FT reconstruction, an alternative measure can be performed by selecting photons detected in the FT and correlating their time to the event start time determined from other particles detected in CLAS12. This analysis was performed for events with an electron detected in the CLAS12 Forward Detector whose start time is determined based on the FTOF system and a photon detected in the FT with energy greater than 500 MeV, cluster seed energy greater than 300 MeV, and cluster size greater than or equal to 4 crystals. The photon FT time

projected back to the event vertex was correlated with the event start time as shown in Fig. 38. A Gaussian fit to the distribution gives $\sigma \sim 150$ ps, slightly larger but consistent with the electron timing resolution.

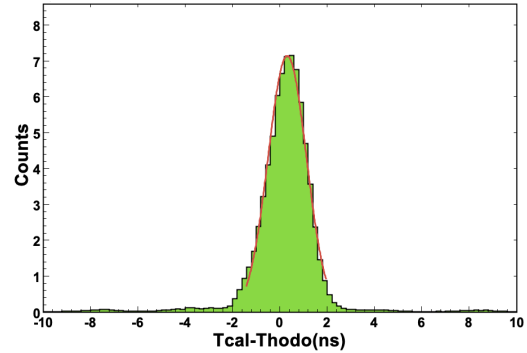


Figure 39: Time difference between the calorimeter and hodoscope clusters for reconstructed electrons. The Gaussian fit to the distribution gives $\sigma \sim 0.8$ ns.

While the FT hit time is determined by the calorimeter since this is the component with the best timing resolution, the time correlation between the individual FT detectors is important to match the signals detected in the three sub-components and minimize accidentals. Figure 39 shows the time difference of the reconstructed calorimeter and hodoscope clusters for detected electrons with $\sigma \sim 0.8$ ns, dominated by the hodoscope resolution. The value is consistent with the design resolution for the hodoscope of < 1 ns.

8.4. Trigger Performance

The FT is used as an active component of the CLAS12 trigger system to identify events in which electrons or photons are detected in the system. This is achieved by reconstructing in real time clusters in the calorimeter with or without geometrical and time matching with hodoscope tiles. Details on the trigger algorithms, their implementation, and validation are provided in Ref. [20], while here we focus only on reporting the performance in terms of linearity of the trigger rate as a function of luminosity. This was studied performing a luminosity scan and recording the FT trigger rate at the input of the data acquisition system. Figure 40 shows the measured dependence. These results confirm the linearity of the FT trigger up to the maximum luminosity foreseen for the experiment.

9. Conclusions

This paper describes the layout and performance of the CLAS12 Forward Tagger. This system was de-

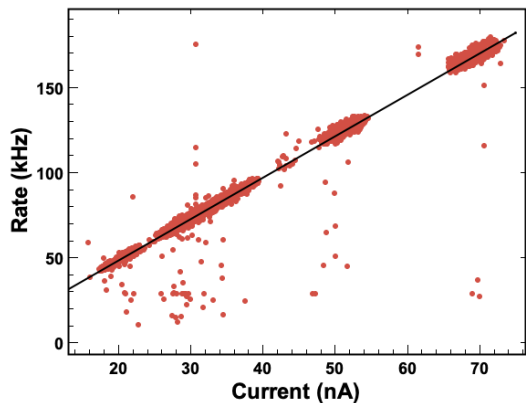


Figure 40: FT trigger rate as a function of the beam current. The measurements are consistent with a linear dependence up to the maximum CLAS12 luminosity of $10^{35} \text{ cm}^{-2} \text{ s}^{-1}$, which is obtained at a current of 75 nA on a 5-cm-long liquid-hydrogen target. The points that deviate from the linear slope correspond to measurements with unstable beam conditions.

signed to detect electrons scattered at very small angles, 2.5° to 4.5° , and to perform measurements of hadronic reactions in the kinematics of quasi-real photoproduction. In this regime, the virtual photon exchanged by the electron interaction with the target has very low four-momentum transfer Q^2 and can be considered as a real photon. These kinematics are ideally suited for the study of hadron production and spectroscopy, extending the physics reach of the CLAS12 experiment beyond its original scope.

The Forward Tagger, composed of an electromagnetic calorimeter for electron detection and energy measurements, a hodoscope to distinguish electrons from photons, and a tracker to precisely measure the electron scattering plane, was designed to be permanently installed in CLAS12 as an integral part of the beamline. After extensive simulation and detector prototyping studies, the three Forward Tagger detectors were assembled and tested separately prior to integration and installation in CLAS12. Upon installation, the full system was commissioned first with cosmic ray data taking and then with beam during the CLAS12 engineering run. These studies enabled us to optimize the detector configuration and to consolidate the calibration procedures for all system components before the start of physics experiments with CLAS12.

The system response has been studied based on different physics reactions to determine acceptance, energy and timing resolution, and trigger performance. While further improvements are expected based on refinements of the calibration procedures and reconstruction algorithms, the Forward Tagger performance is

qualitatively in agreement with the system design specifications, enabling the physics program for which this detector system was designed.

Acknowledgments

The authors would like to thank the engineering and technical staff of Jefferson Lab, the Italian Istituto Nazionale di Fisica Nucleare, the University of Edinburgh, and the University of Glasgow, for their effort and support during the design, construction, and operation of the Forward Tagger. Special thanks to Gianni Nobili, Andrea Rottura, and Diego Torazza for their assistance in this project. Many achievements in the development of the Forward Tagger system would have not been possible without the support of Nathan Baltzell, Sergey Boyarinov, Chris Cuevas, Gagik Gavalian, Ben Raydo, Maurizio Ungaro, and Veronique Ziegler. This work was supported in part by the Italian Istituto Nazionale di Fisica Nucleare, the Scottish Universities Physics Alliance (SUPA), the United Kingdom's Science and Technology Facilities Council, the French Commissariat à l'Énergie Atomique, the U.S. Department of Energy, Office of Science, Office of Nuclear Physics under contract DE-AC05-06OR23177, and the National Science Foundation under grant NSF PHY-1229373.

References

- [1] M. Battaglieri, et al., E12-11-005, Meson Spectroscopy with low Q^2 electron scattering in CLAS12, a CLAS Collaboration proposal to PAC37 (2011).
- [2] V. D. Burkert, et al., The CLAS12 Spectrometer at Jefferson Laboratory, to be published in Nucl. Instrum. Meth. A, (2020). (See this issue) (2020).
- [3] S. Boyarinov, et al., The CLAS12 data acquisition system, to be published in Nucl. Instrum. Meth. A, (2020). (See this issue) (2020).
- [4] Y. G. Sharabian, et al., The CLAS12 high threshold Cerenkov counter, to be published in Nucl. Instrum. Meth. A, (2020). (See this issue) (2020).
- [5] R. Fair, et al., The CLAS12 Superconducting Magnets, to be published in Nucl. Inst. and Meth. A, (2020) (see this issue) (2020).
- [6] M. D. Mestayer, et al., The CLAS12 drift chamber system, to be published in Nucl. Instrum. Meth. A, (2020). (See this issue) (2020).
- [7] CMS Collaboration, The Electromagnetic calorimeter project: Technical Design Report, CERN-LHCC-97-33 (1997).
- [8] F. X. Girod, et al., Measurement of Deeply Virtual Compton Scattering Beam-Spin Asymmetries, Phys. Rev. Lett 100 (2008) 162002.
- [9] PANDA Collaboration, Technical Design Report for the PANDA Forward Spectrometer Calorimeter, arXiv:1704.02713 (2017).

- 1488 [10] T. Horn, et al., Scintillating crystals for the Neutral Particle
1489 Spectrometer in Hall C at JLab, arXiv:1911.11577 (2019).
- 1490 [11] E. Auffray, et al., Performance of ACCOS, an automatic crystal
1491 quality control system for the PWO crystals of the CMS
1492 calorimeter, Nucl. Instrum. Meth. A 456 (2001) 325–41.
- 1493 [12] S. Fegan, et al., Assessing the performance under ionising radiation
1494 of lead tungstate scintillators for EM calorimetry in the
1495 CLAS12 Forward Tagger, Nucl. Instrum. Meth. A 789 (2001)
1496 101–108.
- 1497 [13] A. Celentano, et al., Design and realization of a facility for
1498 the characterization of Silicon Avalanche PhotoDiodes, JINST
1499 9 T09002 (2014).
- 1500 [14] M. Battaglieri, et al., CLAS12 Forward Tagger (FT) Technical
1501 Design Report, <http://www.ge.infn.it/~batta/jlab/ft-tdr.2.0.pdf>
1502 (2012).
- 1503 [15] A. Acker, et al., The CLAS12 Micromegas vertex tracker, to be
1504 published in Nucl. Instrum. Meth. A, (2020). (See this issue)
1505 (2020).
- 1506 [16] S. Stepanyan, et al., The CLAS12 beamline and its performance,
1507 to be published in Nucl. Instrum. Meth. A, (2020). (See this issue)
1508 (2020).
- 1509 [17] M. Ungaro, et al., The CLAS12 Geant4 simulation, to be published
1510 in Nucl. Instrum. Meth. A, (2020). (See this issue) (2020).
- 1511 [18] G. M. B. Buonomo, P. Valente, Performance and upgrade of the
1512 DAFNE Beam Test Facility (BTF), IEEE Trans. Nucl. Sci. 52
1513 (2005) 824.
- 1514 [19] V. Ziegler, et al., The CLAS12 software framework and event reconstruction,
1515 to be published in Nucl. Instrum. Meth. A, (2020).
1516 (See this issue) (2020).
- 1517 [20] S. Boyarinov, et al., The CLAS12 trigger system, to be published
1518 in Nucl. Instrum. Meth. A, (2020). (See this issue) (2020).
- 1519 [21] E. Fanchini, et al., FT calorimeter response to cosmic ray data
1520 during the pre-commissioning phase, CLAS12- Note 2016-005.
1521 [https://misportal.jlab.org/mis/physics/clas12/
1522 viewFile.cfm/2016-005.pdf?documentId=31](https://misportal.jlab.org/mis/physics/clas12/viewFile.cfm/2016-005.pdf?documentId=31) (2016).
- 1523 [22] E. Fanchini, et al., FT calorimeter response to cosmic ray
1524 during the commissioning phase at JLab with
1525 high and low gain preamplifiers, CLAS12-Note 2017-006.
1526 [https://misportal.jlab.org/mis/physics/clas12/
1527 viewFile.cfm/2017-006.pdf?documentId=41](https://misportal.jlab.org/mis/physics/clas12/viewFile.cfm/2017-006.pdf?documentId=41) (2017).
- 1528 [23] D. S. Carman, et al., The CLAS12 Forward Time-of-Flight System,
1529 to be published in Nucl. Instrum. Meth. A, (2020). (See this
1530 issue) (2020).